Cerebral Cortex, December 2017;27: 5784–5803

doi: 10.1093/cercor/bhx261
Advance Access Publication Date: 13 October 2017
Original Article

ORIGINAL ARTICLE

Optogenetic Modulation of a Minor Fraction of Parvalbumin-Positive Interneurons Specifically Affects Spatiotemporal Dynamics of Spontaneous and Sensory-Evoked Activity in Mouse Somatosensory Cortex in Vivo

Jenq-Wei Yang[1], Pierre-Hugues Prouvot[2,3], Vicente Reyes-Puerta[1], Maik C. Stüttgen[4], Albrecht Stroh[2,3] and Heiko J. Luhmann[1]

[1]Institute of Physiology, University Medical Center of the Johannes Gutenberg University Mainz, Duesbergweg 6, D-55128 Mainz, Germany, [2]Institute for Microscopic Anatomy and Neurobiology, University Medical Center of the Johannes Gutenberg University Mainz, Duesbergweg 6, D-55128 Mainz, Germany, [3]Focus Program Translational Neuroscience, University Medical Center of the Johannes Gutenberg University Mainz, Duesbergweg 6, D-55128 Mainz, Germany and [4]Institute of Pathophysiology, University Medical Center of the Johannes Gutenberg University Mainz, Duesbergweg 6, D-55128 Mainz, Germany

Address correspondence to Heiko J. Luhmann, Institute of Physiology, University Medical Center of the Johannes Gutenberg University, Duesbergweg 6, D-55128 Mainz, Germany. Email: luhmann@uni-mainz.de

Jenq-Wei Yang and Pierre-Hugues Prouvot contributed equally to this work.
Heiko J. Luhmann and Albrecht Stroh equal contribution as last authors.

Abstract

Parvalbumin (PV) positive interneurons exert strong effects on the neocortical excitatory network, but it remains unclear how they impact the spatiotemporal dynamics of sensory processing in the somatosensory cortex. Here, we characterized the effects of optogenetic inhibition and activation of PV interneurons on spontaneous and sensory-evoked activity in mouse barrel cortex in vivo. Inhibiting PV interneurons led to a broad-spectrum power increase both in spontaneous and sensory-evoked activity. Whisker-evoked responses were significantly increased within 20 ms after stimulus onset during inhibition of PV interneurons, demonstrating high temporal precision of PV-shaped inhibition. Multiunit activity was strongly enhanced in neighboring cortical columns, but not at the site of transduction, supporting a central and highly specific role of PV interneurons in lateral inhibition. Inversely, activating PV interneurons drastically decreased spontaneous and whisker-evoked activity in the principal column and exerted strong lateral inhibition. Histological assessment of transduced cells combined with quantitative modeling of light distribution and spike sorting revealed that only a minor fraction (~10%) of the local PV population comprising no more than a few hundred neurons is optogenetically modulated, mediating the observed prominent and widespread effects on neocortical processing.

Key words: cerebral cortex, connectivity, interneurons, mouse, optogenetics, parvalbumin

Introduction

In rodents, whiskers represent one of the main sensory modalities to explore the external environment (Schiffman et al. 1970), in addition to auditory and olfactory systems. Tactile information is transduced by the mechanoreceptors located in whisker follicles, and then transferred via ascending pathways including brain stem and thalamus. Whisker-responsive neurons in the ventroposteromedial nucleus of the thalamus project mainly to layer IV of the vibrissal area of primary somatosensory cortex (S1), also referred to as barrel cortex (Van der Loos and Woolsey 1973; Pouchelon et al. 2014). Deflection of an individual whisker leads to the activation of a single corresponding barrel in S1. Each barrel-related column is comprised of a functional ensemble of neural circuits, subdivided into granular (layer IV), supragranular (layers I, II/III) and infragranular layers (V and VI). Within a barrel column, the majority of neurons are excitatory, only between 10% and 20% are inhibitory (Lefort et al. 2009; Meyer et al. 2011).

Inhibitory neurons represent a morphologically and functionally very diverse neuronal entity in the neocortex. Out of this heterogeneous population, interneurons expressing the calcium-binding protein parvalbumin (PV) represent a substantial fraction of about 40% of all GABAergic interneurons (Rudy et al. 2011). The axons of the majority of PV interneurons form basket-like arrangements around the cell bodies and dendrites of pyramidal neurons, and are therefore also referred to as "basket cells." Upon depolarization, they fire high-frequency spike trains and exhibit little to no firing rate adaptation (Gentet 2012). Beyond providing inhibition to local principal cells, PV cells may also inhibit neurons located several hundred micrometers away (Helmstaedter et al. 2009; Kätzel et al. 2011). Importantly, these neurons are thought to constitute a subnetwork connected by electrical synapses, allowing for the rapid synchronization of activity (Galarreta and Hestrin 1999).

In visual cortex, PV interneurons have been implicated in processes such as response gain control (Atallah et al. 2012) and response reliability (Zhu et al. 2015), yet their specific role in shaping the spatiotemporal dynamics of sensory representations in somatosensory cortex is unknown. Mechanistically, experimental evidence indicates that PV interneurons can provide strong somatic feedforward inhibition, therefore, directly affecting spiking output of the excitatory network in barrel cortex (Sun et al. 2006) and auditory cortex (Li et al. 2014, 2015). Functional studies using local field potential (LFP) recordings in PV (–/–) knockout mice show higher synchronous activity both in the neocortex and hippocampus, accompanied by an increased susceptibility to epileptic seizures (Schwaller et al. 2004), yet life-long knockouts of functional compartments of a network may result in circuit rearrangements, not allowing to further our understanding the role of a given neuronal population under physiological conditions.

Optogenetics allows a temporally and spatially precise manipulation of distinct components of the neuronal network, avoiding circuit rearrangements that may occur, for example, in knockout mice (Boyden et al. 2005; Deisseroth 2015). Both, excitation of neurons using mainly light-sensitive cation channels, as well as inhibition using light-driven pumps, such as the proton pump ArchT (Han et al. 2011), the chloride pump NpHR (Zhang et al. 2007), or light-sensitive chloride channels (Berndt and Deisseroth 2015; Govorunova et al. 2015) became feasible.

In mouse barrel cortex, optogenetic activation of PV interneurons at gamma frequencies induces gamma oscillations in the entire network as recorded with LFPs and changes the evoked response following whisker stimulation including number of spikes, response latency, and spike precision (Cardin et al. 2009). In addition, a recent study found an enhancement of behavioral performance in a simple detection task upon optogenetic inhibition of PV interneurons (Sachidhanandam et al. 2016). However, assessing the spatiotemporal scope of the impact of PV interneurons on the encoding of sensory afferents in a highly spatially organized structure such as the barrel cortex requires an assessment of both the density of optogenetically modulated PV interneurons and the geometry of light distribution in brain tissue. Notably, while optogenetics has just celebrated its first decade, the scope of the optogenetic network modulation in terms of the relative number of activated cells has been subject of only a few specific studies (Aravanis et al. 2007; Huber et al. 2008; Yizhar et al. 2011; Schmid et al. 2016). However, an assessment of the impact of a defined number of interneurons on the spatiotemporal computation of whisker-evoked cortical activity has not been achieved up to now.

Here we combine optogenetics with spatially resolved multielectrode recordings in mouse barrel cortex in vivo, complemented by an assessment of the local density of inhibited neurons. We resolve 3 distinct functional components of the network: LFP, reflecting subthreshold synaptic activity and suprathreshold action potential firing, multiunit activity (MUA), reflecting only suprathreshold activity, and lastly single units, allowing for the differentiation between putative excitatory and inhibitory neurons (Reyes-Puerta, Sun et al. 2015).

In the lightly anesthetized mouse expressing ArchT or ChR2 in PV interneurons (ArchT/PV or ChR2/PV mice) in layers II/III and V, we record spontaneous and single-whisker evoked activity upon optogenetic modulation. We correlate the functional findings with an estimation of the relative density of optogenetically modulated neurons. We find that a small number of light-modulated PV interneurons exert control over a large number of excitatory and inhibitory neurons, extending to neighboring barrel columns and affecting both spontaneous activity over a broad frequency range as well as shaping the spatiotemporal dynamics of whisker-evoked neuronal activity.

Materials and Methods

Animals

All procedures related to the care and treatments of animals were approved by a local ethics committee (#23 177-07/G10-1-010) and followed the European and German national regulations (European Communities Council Directive, 86/609/EEC). A total of 18 PV-Cre mice (13 males and 5 females, 1.5–9 months, B6, 129P2-Pvalb, Ref. 017 320, Jackson laboratories) were used for photoinhibition experiments. Six PV-Cre mice (male, 4–5 months) were used for photoactivation experiments. Three C57BL/6 mice (male, 1–1.5 months) and 6 PV-Cre mice (4 males, 2 females, 2–4.5 months) were used for testing the photoelectrical effect on the LFP. In total, 13 PV-Cre mice (6 males, 7 females, 2–10 months) were used for immunohistochemistry.

Virus Injection

Injections of viral solutions were conducted under deep isoflurane anesthesia (Forene, Abbott, Wiesbaden, Germany). PV-Cre mice were placed on a warming pad (37 °C) and fixed in a stereotactic frame (Kopf Instruments). At the level of the somatosensory cortex (AP: −2 mm, ML: 3.5 mm), the skull was thinned with a dental drill (Ultimate XL-F, NSK, Trier, Germany), and a small cranial opening was prepared under a dissecting microscope using a small injection needle. Viral solutions containing 2×10^{11} viral particles per ml, rAAV2-FLEX-ArchT-GFP, rAAV2-FLEX-ArchT-tdTomato, or rAAV2-FLEX-ChR2-mCherry in PBS were delivered by a glass micropipette with microliter graduations (Hirschmann Laborgeräte, Eberstadt, Germany) pulled by a horizontal puller (Sutter Instruments, Novato, CA) connected to a 10 ml syringe by manual pressure (for details see Fois et al. 2014). About 300 nl viral solution (0.6×10^{8} viral particles) were slowly injected within 3 min at 300 and 600 µm cortical depth from the pia before slowly retracting the pipette. Functional experiments were conducted no earlier than 2 weeks after surgery.

Surgical Preparation, Multielectrode Recordings and Whisker Stimulation

Extracellular in vivo recordings were performed in the barrel cortex 1–3 months after virus injection. The mouse was anesthetized using urethane (1.5 g/kg, intraperitoneal injection), head-fixed in a stereotactic frame and placed on a warming pad at a constant body temperature of 37 °C. During recording, additional urethane (10–20% of the initial dose) was given when the mice showed any sign of distress. A silver wire was inserted into the cerebellum as ground electrode. A 2×2 mm^2 craniotomy was performed over the barrel cortex, centered at the previous small craniotomy of virus injection. According to the location of the previous virus injection, an 8-shank 128-channel electrode (200 µm horizontal shank distance and 75 µm vertical interelectrode distance, impedances 1–2 MΩ, NeuroNexus Technologies, Ann Arbor, MI) or 4-shank 80-channel electrode (150 µm horizontal shank distance and 50 µm vertical interelectrode distance, 1–2 MΩ) was inserted perpendicularly into the barrel cortex to record the LFP and MUA (Fig. 1A). After 60–90 min of electrode insertion, single whisker stimulation was performed to identify the targeted barrel columns. A single whisker was stimulated using a miniature solenoid actuator (modified from Krupa et al. 2001). The movement of the tip of the stimulator bar was measured precisely using a laser micrometer (MX series, Metralight, CA, USA) with 2500 Hz sampling rate. The stimulus takes 26 ms to reach the maximal 1 mm whisker displacement, with a total duration of 60 ms until it reaches baseline. Because the single whisker was stimulated approximately 2 mm distal from the base, the peak stimulus velocity is 1114°/s. In addition to the 1 mm whisker displacement, we also use 0.4 and 1.6 mm whisker displacement to test the effect of different stimulus strengths on the evoked response amplitude during the PV interneuron inactivation (Supplementary Fig. 7). The positioning of the principal shank (PS) electrode in the center of the transduced area was confirmed in all experiments by postmortem confocal analysis (Fig. 1 and 2).

Optical Stimulation Setup

The light for excitation of ArchT was delivered by a 60 mW solid-state laser at 552 nm wavelength (Sapphire, Coherent, Dieburg, Germany), and for ChR2 stimulation, a 50 mW solid-state laser at a wavelength of 488 nm (Sapphire, Coherent, Dieburg, Germany) was used. Both lasers were placed in a custom-built optical setup. The laser beams were coupled to a

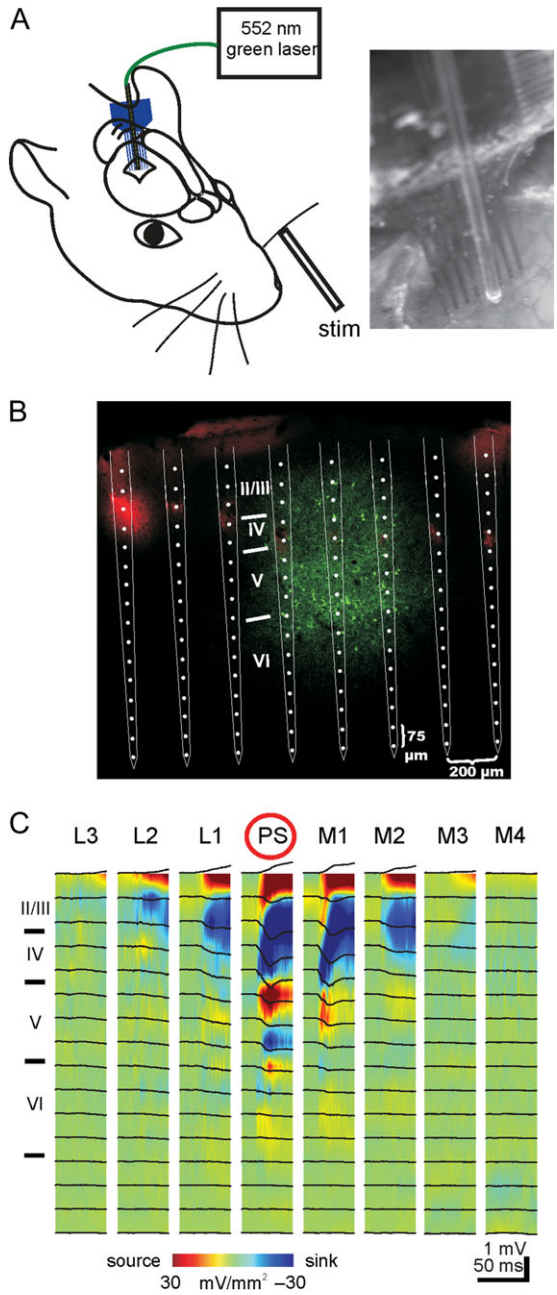

Figure 1. Experimental setup for combining in vivo multielectrode recordings, optogenetic manipulation and mechanical stimulation of single whiskers in adult mice. (*A*) Schematic illustration of the experimental setup for data recording using 8-shank 128-channel probes, selective mechanical stimulation of a single whisker and photo-illumination using an optical fiber connected to a 552 nm green laser. Right panel shows a photograph of the cortical surface with electrode array and optical fiber. (*B*) Fluorescent image of ArchT-GFP expression pattern (green) and position of DiI-covered electrode tracks (red). An 8-shank 128-channel electrode probe is superimposed on this image according to the position of the DiI tracks. (*C*) Local field potential responses (black lines) and corresponding color-coded current-sink-source density (CSD) depth profile following stimulation of whisker E1. Blue color represents current sinks and red color represents current sources. The shank showing the largest stimulus-evoked response amplitude was located in the E1-column and denoted the principal shank (PS). Activity profiles recorded at electrodes located lateral (L) and medial (M) from the PS are also illustrated.

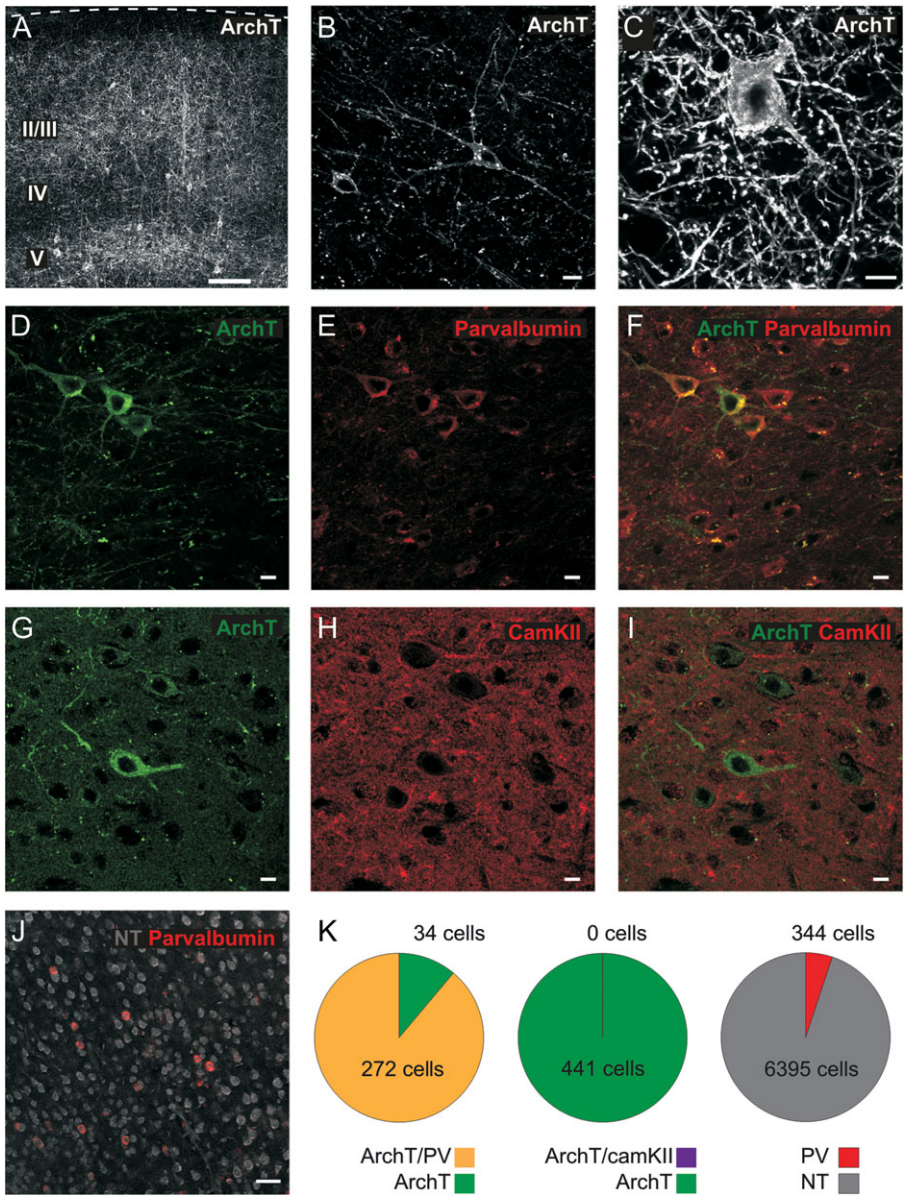

Figure 2. Layer and cell type specificity of ArchT expression in mouse barrel cortex. (*A–C*) Confocal micrographs of coronal sections of somatosensory cortex from PV-cre mice injected with AAV-floxed-ArchT-tdTomato/GFP reveal ArchT expressing cells mainly confined to layers II/III and V. Scale bars: 100 µm in *A* and 10 µm in *B* and *C*. (*D–F*) ArchT-GFP-expressing cells (green, *D*); PV-expressing cells (anti-PV immunostaining, red, *E*); merged photo from *D* and *E*. Scale bars: 10 µm. (*G–I*) ArchT-GFP-expressing cells (green, *G*); co-staining with anti-CamKII (red, *H*); merged photo from *G* and *I*. Scale bars: 10 µm. (*J*) Co-staining with a fluorescent Nissl stain (Neurotrace) and a Parvalbumin antibody. Scale bar: 50 µm. (*K*) Pie charts depicting the ratios of co-stainings: left ArchT/PV (90.9 ± 2.8%, from 4 mice), middle ArchT/CamKII (0%, from 3 mice), right PV/NT (5.9 ± 0.7%, from 2 mice).

200 µm multimode fiber with a numerical aperture of 0.39 (Thorlabs, Munich, Germany) by means of a fiber collimator (Schäfter + Kirchhoff, Hamburg, Germany). To ensure reproducibility of the power density used, the output power at the end of the fiber was measured prior to each experiment with a powermeter (Nova 2, Ophir, Newport, Irvine, CA). The initial power density was calculated with $I_0 = i/\pi r^2$, where i is the initial power and r the radius of the fiber core (0.1 mm). The light pulsing was controlled by a mechanical shutter (Uniblitz, Rochester USA) connected to a stimulator (Master8, A.M.P.I., Jerusalem, Israel). The fiber was positioned parallel to the electrodes by means of a micromanipulator and barely touched the cortical surface (Fig. 1A).

LFP and MUA Analysis

For the ArchT experiments, we observed optically induced artifacts in our LFP recordings independent of ArchT, brought about by photons interacting with electrons in the metallic recording probe, termed Becquerel or photoelectric (PE) effect, as already reported by others (Cardin et al. 2010; Laxpati et al. 2014). To assess the scope of optically induced artifacts, we performed control experiments in 3 wild type mice and 6 PV-Cre mice without ArchT expression. Light illumination (100 ms, 150 mW/mm^2) altered evoked LFP recordings following single whisker stimulation. The PE effect was most notable in the 3 upper electrodes, corresponding to layer I and upper layer II/

III (Supplementary Fig. 3A). We systematically compared the effects of different filtering settings (1, 2, 3, 4, 8 Hz high-pass filtering) on the evoked LFP and found 4 Hz high-pass filtering almost entirely compensate for the PE effect (Supplementary Figs 2 and 3B). Light illumination (1 s, 150 mW/mm^2) also altered spontaneous LFP recordings. Fast Fourier transform (FFT) analysis shows a clear effect on the delta band (Supplementary Fig. 1A). Again, 4 Hz high-pass filtering removed the PE effect in spontaneous LFP recordings (Supplementary Fig. 1B). However, to minimize any potential contamination of our data, we used only electrodes located in deep layer II/III for our analysis, barely affected by the PE effect, but applied 4 Hz high-pass filtering to all data.

For the ChR2 experiments, activating PV interneurons induced very large LFP responses at the very onset of illumination, representing the strong initial response (Stroh et al. 2013), strongly influencing the calculation of evoked LFP peaks. To overcome this issue, we additionally performed illumination without sensory stimulation. We then subtracted this early nonsensory-related component of the LFP response from the sensory-evoked LFP response.

Data were imported and analyzed offline using MATLAB software version 7.7 (Mathworks, Natick, MA, USA). MUA was extracted from 800 to 5000 Hz filtered raw signals by applying a threshold at 7.5 times the baseline standard deviation (SD).

Current Source Density Analysis

Current source density (CSD) depth profiles were calculated from averaged sensory-evoked LFP responses. First, we duplicated the LFP traces in the uppermost and lowermost channels of each shank. One-dimensional CSD profiles were then calculated from the LFP according to a 3-point formula (Freeman and Nicholson 1975). The CSD values I_m were derived from the second spatial derivative of the extracellular field potentials f and calculated by the finite-difference formula:

$$I_m = -\frac{[f(x-h) - 2f(x) + f(x+h)]}{h^2},$$

where, h is the distance between successive measuring points (75 µm for 8-shank 128-channel electrode arrays and 50 µm for 4-shank 80-channel electrode arrays) and x is the coordinate perpendicular to the cortical layer. In the CSD profiles, current sinks are indicated by downward deflections and sources by upward deflections. To facilitate visualization of CSD profiles, we generated color image plots by linear interpolation along the depth axis. The blue color represents current sinks and red color represents current sources (Fig. 1C).

Up State Detection

The slow oscillations (Up–Down state transitions) were detected by the method described by Compte et al. (2008). Briefly, LFPs in layer II/III were used to identify Up and Down states. First, raw LFP was down-sampled to 1 kHz. Second, the envelope of the LFP (Supplementary Figs 4 and 6A, dashed trace) was calculated by Hilbert transform and further smoothed using a 100 ms moving average. Third, the 1.5-fold of mean value of the envelope was employed as the threshold (Supplementary Figs 4A and 6A, blue line) for the detection of transitions between Up and Down states. Up states shorter than 50 ms were discarded.

Spike Detection and Sorting

Spike detection and sorting were performed as described in detail previously (Reyes-Puerta, Kim et al. 2015; Reyes-Puerta, Sun et al. 2015). First, the raw data were high-pass filtered (0.8–5 kHz). Nonoverlapping groups of 2–4 channels were selected and at least one channel was left unused between neighboring groups to ensure that a sorted unit was present only in one group. Spike detection was performed in each recorded channel independently using 7.5-times the standard deviation of the signal. When a threshold crossing was detected in either of the channels within a group, all sampled amplitude values from all channels in the time range from −0.5 to +0.5 ms relative to the waveform negative peak were extracted. These spike waveforms were then used to compute feature vectors (negative peak amplitude and 2 first principal components derived from the waveforms). The feature vectors were then used to perform spike sorting using KlustaKwik and Klusters (Harris et al. 2000; Hazan et al. 2006). Several criteria were used to ensure the isolation quality of the sorted neurons (for details see Reyes-Puerta, Kim et al. 2015; Reyes-Puerta, Sun et al. 2015). Cells were subsequently classified as putative inhibitory (INH) interneurons or putative excitatory (EXC) pyramidal neurons based on the mean spike waveform (Fig. 10C, D). For each neuron, 3 parameters were calculated and used to separate INHs and EXCs by k-mean clustering method: (1) spike half-with (ms), (2) the trough to right (late) peak latency, and (3) asymmetry index (Supplementary Fig. 10).

Histology and Immunohistochemistry

After the electrophysiological experiments, mice were transcardially perfused with 4% paraformaldehyde (PFA) under deep isoflurane anesthesia to characterize the opsin expression. Brains were removed, fixed overnight in 4% PFA, and transferred to 30% sucrose solution. Coronal brain sections of 70 µm thickness were prepared using a vibratome (Leica, Wetzlar, Germany). For permeabilization, slices were incubated with 0.1% Triton X-100 and 5% normal donkey serum (Invitrogen, Life Technologies, Carlsbad, CA) in phosphate buffer solution for 90 min. Slices were incubated with goat anti-PV (1:200, Swant, Marly, Switzerland) or rabbit anti-CamKII (1:200, Epitomics, Burlingame, CA) at 4 °C overnight. On the next day, slices were incubated with the secondary antibodies Cy-2 donkey anti-goat (1:200, Jackson Immuno Research, West Grove, PA), or Cy-2 donkey anti-rabbit (1:200, Jackson Immuno Research, West Grove, PA), and a fluorescent Nissl stain (red 615 nm, Neurotrace, Molecular Probes, Life Technologies, Carlsbad, CA). Slices were mounted using antiquenching Vectashield (Vector Laboratories, Burlingame, CA).

Quantification of Number and Densities of Illuminated Cells

To assess the number and density of optogenetically inhibited cells, we first imaged the area of expression in coronal brain slices of 5 mice using a confocal microscope (SP8, Leica, Mannheim, Germany) and a ×20 objective (HCX PL APO dry, Leica), with a numerical aperture of 0.70. Expression was confined to layers II/III and V, only very few cells could be observed in layer IV, in line with previous studies (Stroh et al. 2013; Schmid et al. 2016). Next, we quantified neurons exhibiting strong, membrane-bound ArchT-tdTomato (n = 3 mice) or ArchT-GFP (n = 2 mice) or ChR2-mCherry (n = 5 mice) fluorescence

using an epifluorescence microscope (Olympus BX51, Japan, equipped with a ×20 NA = 0.75 UPlanSApo Olympus objective) and dedicated software (StereoInvestigator, Microbrightfield, Williston, USA) in a randomized approach (Schmid et al. 2016). The quantifications resulted in average cell densities in layers II/III and layer V, as stated in the results section.

We then estimated the minimal photocurrent needed to effectively silence ArchT expressing PV interneurons. Considering a typical membrane resistance of R_m = 90 MΩ (Galarreta and Hestrin 2002) and assuming that a membrane potential hyperpolarization of 25 mV is required for action potential inhibition, a photocurrent of at least 250 pA is required in this case. For ArchT (Han et al. 2011), this inward photo current is reached at about 1.5 mW/mm^2 illumination density.

We estimated the light power density sufficient for effective ChR2 activation according to Prigge et al. (2012). They demonstrated, that light power densities as low as 0.875 mW/mm^2 reliably evoked spiking in cultured pyramidal neurons expressing ChR2. With 45 mW/mm^2 as initial power at the fiber tip, this density is reached about 650 µm in depth of the tissue. Indeed, we can identify spiking responses in our MUA data upon illumination with 45 mW/mm^2 up to a depth of 675 µm (Supplementary Fig. 11).

We used 2 models for assessing the light density distribution in brain tissue: the spherical model (Schmid et al. 2016), as an extreme example of lateral scattering, and the Kubelka–Munk-model, underestimating lateral scattering, but more realistic for penetration depth. In layer II/III, the spherical model results in an area of above-threshold light illumination with a lateral radius of 380 µm, exceeding the lateral spread of ArchT expression of 320 ± 10 µm. Consequently, the entire layer II/III expressing volume (0.097 ± 0.007 mm^3) is effectively illuminated. Assuming a conical spread of light from the tip of the fiber following the Kubelka–Munk model, the area of above-threshold illumination comprises of a frustrum with an upper radius of 100 µm and a lateral angle of 18.5° with NA = 0.39, refractive index, n_i = 1.36 for mouse grey matter. Applying a power density of 150 mW/mm^2 at the fiber tip, the inhibition threshold of 1.5 mW/mm^2 is reached at a distance of 800 µm in dorsoventral direction.

The area of ArchT expression commences at layer II/III at about 100 µm of cortical depth, ceasing at around 430 µm. This results in an efficiently inhibited volume of 0.0376 mm^3 in layer II/III, which is considerably smaller than the volume of expression (0.097 ± 0.007 mm^3). In layer V, the volume efficiently illuminated is larger than the volume of expression for ArchT (0.0684 ± 0.0041 mm^3), therefore we can assume inhibiting the entire expressing population in layer V. The actual cell numbers were obtained by multiplying the calculated volumes with the measured cell densities. For assessing the relative proportion of ArchT-expressing neurons with regard to the neuronal population of the entire cortical column, we related the volume of the cortical layers harboring ArchT expressing neurons to the volume of the entire column.

For ChR2 stimulation using 45 mW/mm^2 as initial power at the fiber tip, the spherical model results in a lateral radius of 290 µm of effective illumination, amounting to a volume of 0.024 mm^3 in layer II/III. Using the conical model, the volume efficiently stimulated in layer II/III is 0.0376 mm^3. In layer V the volume efficiently illuminated is 0.0863 mm^3, as for ArchT excitation we used only the conical model for layer V, as the spherical model cannot be employed for deeper regions, as described (Schmid et al. 2016).

Data Evaluation and Statistics

Data in the text and figures are presented as means ± SEM. Statistical analyses were performed with GraphPad Prism (GraphPad Software, Inc.; La Jolla, CA, USA) or MATLAB. We performed D'Agostino & Pearson omnibus normality tests to test for normal distribution of the data when appropriate. Paired *t* test and repeated-measures ANOVA were used when the data were normally distributed. The Friedman test, Mann–Whitney–Wilcoxon test and Wilcoxon signed-rank test were used when data exhibited non-Gaussian distributions. The Kolmogorov–Smirnov test was employed to compare 2 non-normal distributions.

Results

Combining Depth-Resolved Multichannel Recordings and Optogenetic Manipulation of PV Interneurons in Mouse Barrel Cortex

The effects of transient PV-mediated disinhibition on neocortical network function were studied by intracortical multielectrode array (MEA) recordings in 18 adult mice in vivo. In barrel cortex of lightly anesthetized mice, we combined 4- or 8-shank multichannel recordings with optic fiber-based optogenetic inhibition of PV interneurons. The electrode shanks were inserted at the site of ArchT expression and in neighboring cortical columns. The optic fiber was then placed parallel to the recording shanks, in the center of the ArchT-expressing area, barely touching the cortical surface (Fig. 1*A*). Electrode shanks were marked with DiI for post hoc identification of recording sites by confocal microscopy. Postmortem histology indicated that electrode shanks indeed penetrated the ArchT-GFP expressing area and covered all cortical layers (Fig. 1*B*). Stimulation of single whiskers was performed alongside multichannel recordings. Only the whisker evoking the maximal response in the middle shank (PS) was retained for subsequent stimulation, all other whiskers were trimmed. CSD analysis allowed the identification of the principal column and cortical layers (Fig. 1*C*). Neighboring electrodes lateral (L) and medial (M) to the PS electrode recorded the activity in the neighboring columns.

Interneuron-Specific Expression of ArchT in Layers II/III and V in Mouse Barrel Cortex

Floxed ArchT-tdTomato encoding AAVs were stereotactically injected in barrel cortex of PV-Cre transgenic mice to achieve selective expression of the inhibitory opsin in PV interneurons. Notably, expression was almost exclusively constrained to layers II/III and V. In layer IV, only very few ArchT-positive neurons could be found, even though it was included in the injection scheme. The area of expression constituted a cylinder with a diameter of 640 ± 20 µm (n = 5 mice), and a dorsoventral extent ranging at 300 µm in layer II/III and 200 µm in layer V (Figs 1*B* and 2*A*). Within this area, neurons exhibited strong, membrane-bound expression of ArchT-tdTomato/-GFP (Fig. 2*B*, *C*).

Next, we assessed the cell type specificity of ArchT expression. Upon immunostaining and quantification of co-expression in confocal micrographs, we identified 90.9 ± 2.8% (n = 272 cells from 4 mice) of the ArchT-expressing neurons as clearly PV-positive (Fig. 2*D*–*F*; *K*, left chart), the remaining cells exhibited only weak PV immunofluorescence. To test for an unspecific expression in excitatory neurons, we conducted a co-staining for anti-CaMKII. Not a single region of ArchT expression contained neurons which were co-stained for both CaMKII and ArchT-tdTomato,

demonstrating the high specificity of viral expression (Fig. 2G–I; K, middle chart; 441 cells in $n = 3$ mice). Lastly, we assessed the relative proportion of PV interneurons in the local neuronal network. Upon staining for neuronal nucleic acids and anti-PV immunofluorescence, a percentage of 5.1 ± 1.5% out of all neurons were PV positive, in line with a previous study (Lefort et al. 2009) (Fig. 2J; K, right panel; $n = 2$ mice, 6395 cells).

Inhibiting PV Interneurons Causes Broad-Spectrum Hyperexcitability

Spontaneous LFPs were recorded in deep supragranular layers by electrodes of the PS, and a 1 s green laser light pulse at 150 mW/mm^2 was applied to the cortical surface every 10 s in ArchT/PV mice. During this transient disinhibition, spontaneous LFPs were enhanced over a broad frequency range from theta up to the gamma band; moreover, this transient network hyperexcitability was associated with a prominent increase in MUA (Fig. 3A, B1). The average FFT power from theta to gamma of the LFP increased significantly during the light-induced disinhibition and rapidly recovered to control level following light offset (Fig. 3B2). This effect was specific to ArchT/PV mice, non-expressing control mice did not show any change in FFT power upon light illumination (Supplementary Fig. 1B). This pronounced rise in spontaneous LFP power was associated with a significant ($P < 0.001$, $n = 9$ mice) increase in the mean firing rate from 6.2 ± 1.2 to 9.9 ± 1.5 Hz during light-induced disinhibition (Fig. 3C). As found for LFPs, the MUA also rapidly reached control values after switching off the light pulse (Fig. 3C). These results demonstrate that a transient inhibition of PV-expressing interneurons causes a strong and rapid increase in synaptic excitation and action potential firing of neurons in supragranular layers. These effects are transient and tightly follow the timing of the light-induced disinhibition. For assessing the impact of activating PV interneurons on spontaneous activity, we performed 5 s of illumination at 45 mW/mm^2 without sensory stimulation in animals injected with AAVs encoding for ChR2. Opposite to the enhancement effect on the FFT power by inhibiting PV interneurons, their activation induced a strong, significant decrease in theta to gamma frequency bands (Supplementary Fig. 4A and B).

Under urethane anesthesia, cortical dynamics show prominent slow oscillations (Up–Down state changes) (Steriade et al. 1993; Reyes-Puerta et al. 2016). To evaluate if inhibiting PV interneurons directly impacts slow oscillations, we used a threshold-based algorithm to identify the onsets of Up states based on the work of (Compte et al. 2008). Indeed, the detected Up states are reflected by MUA firing through all cortical layers (Supplementary Fig. 5), in line with a previous study of ours (Stroh et al. 2013). Notably, of 160 detected Up state onsets in a time window of 1 s during ArchT stimulation, 63 onsets followed the beginning of illumination with a latency of less than 100 ms (Fig. 3D1). The distribution of onsets is significantly different from a homogeneous temporal distribution (Fig. 3D2), which would be assumed if there would be no induction of Up states ($P = 0.031$, 2 sample Kolmogorov–Smirnov test). This strongly suggests that ArchT-mediated inhibition of PV interneurons is capable of inducing Up states, in line with a very recent study (Zucca et al. 2017). Yet, inhibiting PV interneurons did not alter the overall occurrence of Up states, but significantly increases their duration (Supplementary Fig. 6C). We next performed experiments activating PV interneurons using ChR2, see below, and could reduce the occurrence of up states but not their duration (Supplementary Fig. 4C).

To address the question whether a similar increase in excitability can also be observed in sensory-evoked cortical activity, the responsiveness to single whisker stimulation in supragranular layers at the PS under no-light conditions and during transient PV-mediated disinhibition was studied. Indeed, we observed a prominent increase in response amplitude upon illumination with 150 mW/mm^2 green light (Fig. 4A), again only in ArchT/PV mice (Supplementary Fig. 3). The increase in response amplitude during disinhibition was dependent on the light intensity (Fig. 4B, C), but the relative change of response amplitude remained unaffected by the different sensory stimulation strength (Supplementary Fig. 7). Compared with the response under no light condition, at a low intensity of 32 mW/mm^2 the peak amplitude already increased significantly ($P = 0.0048$, $n = 13$ mice) to 223.4 ± 35.8%. Higher intensities of 76, 150 and 299 mW/mm^2 induced a further enhancement of the peak amplitude, and at an intensity of 150 mW/mm^2, the response amplitude increased significantly ($P = 0.0002$, $n = 13$ mice) to 314.8 ± 41.5% during PV-mediated disinhibition. This effect was accompanied by a gradual decrease in the duration of the response from 85.9 ± 9.1% of control at 32 mW/mm^2 to 69.4 ± 7.3% at 299 mW/mm^2 (Fig. 4C, right). Based on these experiments, we have chosen 150 mW/mm^2 for all subsequent optogenetic experiments, to achieve a reliable inhibition and at the same time reduce the probability of unspecific effects (Fois et al. 2014). The decrease in the duration and the sharp increase in the peak response of the LFP indicate that the initial component at 10–30 ms after whisker stimulation is most strongly affected. As spontaneous neocortical activity, sensory-evoked responses also showed a prominent increase in the FFT power over a broad frequency range from theta up to the gamma band (Fig. 4D1) during the 100 ms time window of light illumination (150 mW/mm^2), again only in ArchT/PV mice (Supplementary Fig. 1C, D). The FFT power increased significantly ($P = 0.0002$, $n = 13$ mice) from 6.7 ± 2 × 10^6 μV^2 to 20 ± 4.2 × 10^6 μV^2 during the light-induced disinhibition (Fig. 4D2). In summary, these data demonstrate that spontaneous as well as sensory-evoked activity in barrel cortex are prominently enhanced when PV-expressing interneurons are transiently inhibited. Next, we studied the spatiotemporal dynamics of this disinhibition by recording LFPs and MUA with a MEA covering all cortical layers and several barrel-related columns.

Spatial Profile of Transient PV Inhibition

Under control no-light conditions, mechanical deflection of whisker C1 with a duration of 60 ms (Supplementary Fig. 7) elicited the typical activation pattern to single whisker stimulation with large LFP responses recorded at the PS electrode located in the C1 column (Fig. 5A1). Smaller responses were recorded at the lateral shanks L1–L3 and the medial shanks M1–M4. Identical whisker stimulation with simultaneous PV-mediated disinhibition of the excitatory network evoked at all recording sites much larger LFP responses (Fig. 5A2). Interestingly, an increase of the response peak amplitudes could be also observed at the electrode shanks located up to 600 μm lateral (L1–L3) and up to 600 μm medial (M1–M3) (Fig. 5B, C). These data indicate that the local and transient PV-mediated disinhibition induced a widespread excitability increase, affecting several neighboring columns in barrel cortex.

Whereas the LFP reflects the local synaptic activation, the MUA reveals the suprathreshold activation of neurons located near the recording site. Therefore, the whisker stimulation induced MUA was analyzed under control no-light conditions and during PV-mediated disinhibition (Fig. 5D). Under control, deflection of a single whisker evoked a large MUA response in the activated principal column and smaller responses in the

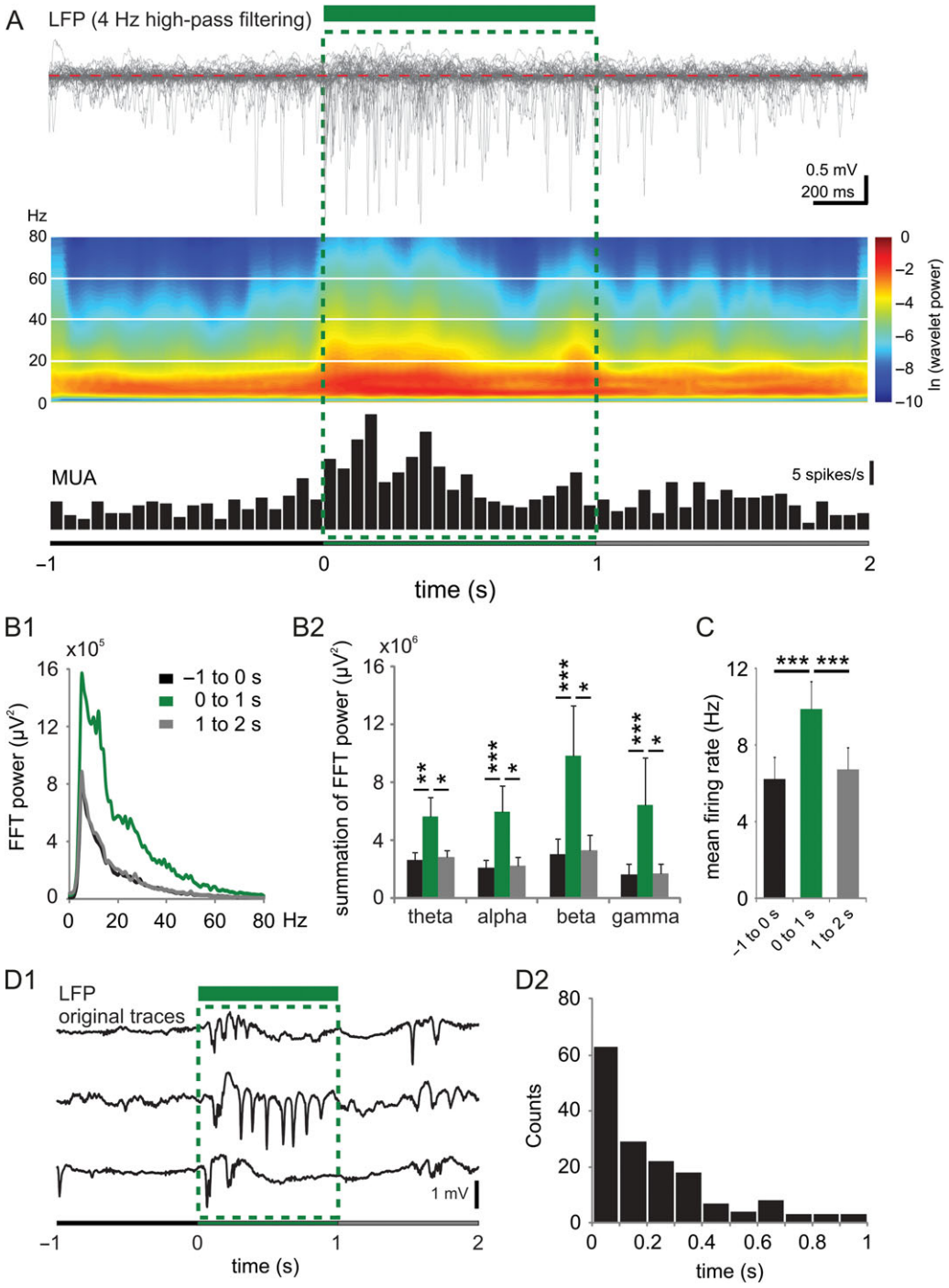

Figure 3. Optogenetic inactivation of PV inhibitory interneurons causes increase in spontaneous neocortical activity. (*A*) Spontaneous LFP activity (4 Hz high-pass filtering) recorded in deep layer II/III at the site of virus transfection before, during (green horizontal bar) and after light stimulation. Upper panel: Fifty superimposed traces of 3 s duration were aligned according to the onset time of the green light pulse (1 s duration, 150 mW/mm^2, every 10 s). Three periods were defined: before (−1 to 0 s), during (0 to 1 s) and after green light pulse (1 to 2 s). Middle panel shows the corresponding wavelet plot averaged from fifty spontaneous LFPs in the upper panel. Lower panel shows corresponding PSTH plot of spontaneous multiunit activity (MUA). (*B1*) Fast Fourier transformation (FFT) of spontaneous LFP activity during the 3 periods (average over 9 animals). Note the prominent and reversible increase of FFT power over a wide frequency band during optogenetic inactivation of PV interneurons (green line). (*B2*) Bar diagram illustrating significant increase of FFT power from theta to gamma band during green light pulse (Friedman test: $^*P < 0.05$, $^{**}P < 0.01$, and $^{***}P < 0.001$). (*C*) Bar diagram showing significant increase of mean firing rate during optogenetic inactivation of PV inhibitory interneurons recorded on the same electrodes (repeated measures ANOVA test: $^{***}P < 0.001$). (*D1*) Three representative unfiltered traces revealing prominently induced slow oscillations during 1 s of inactivating PV interneurons. (*D2*) The temporal distribution of the onsets of slow oscillations upon optogenetic silencing of PV interneurons. A total of 160 events were detected from 9 animals that fulfilled 2 criteria: first, no Up state for at least 500 ms immediately before the onset of illumination; second, occurrence of Up state within the 1 s of illumination.

neighboring columns (Fig. 5*D1*, upper row in Fig. 5*E*). With simultaneous PV-mediated disinhibition at the PS, the maximum MUA response in the principal column did not change in any cortical layer, but interestingly increased at all lateral and medial recording sites (Fig. 5*D2*, lower row in Fig. 5*E* and Supplementary Fig. 8). The spatial MUA profile shows a U-shaped pattern reaching an

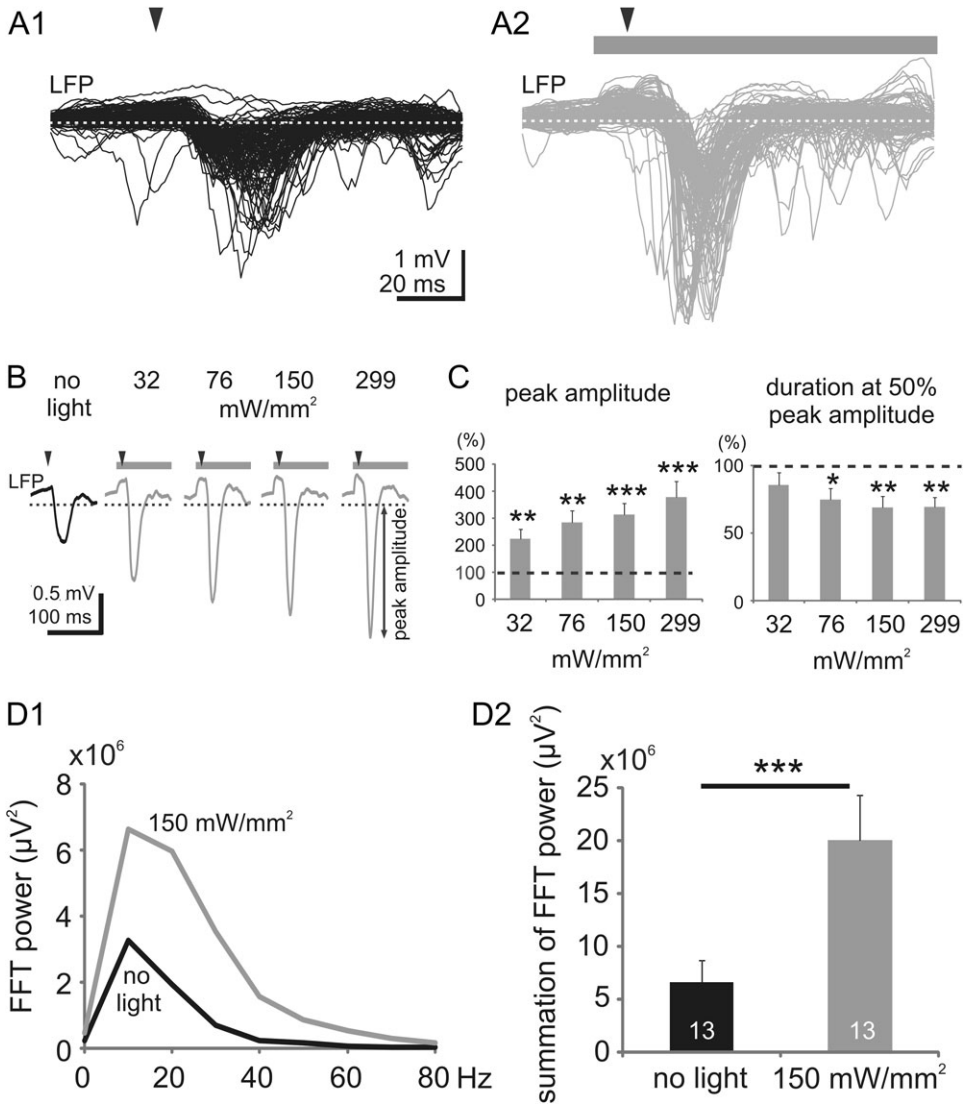

Figure 4. Optogenetic inactivation of PV interneurons causes amplitude and broad spectrum increases in stimulus-evoked cortical responses. (*A*) 130 superimposed traces ($n = 13$ animals) of evoked LFP activity (4 Hz high-pass filtering) recorded in deep layer II/III of the principal barrel column to single whisker stimulation under control condition (A1, no light) and during optogenetic inactivation of PV interneurons (A2, light on, 150 mW/mm^2). In this and the following figures, downward arrowheads indicate time point of single whisker deflection. The dashed lines mark baseline of LFP recordings. (*B*) Enhancement of sensory-evoked response in layer II/III to increasing laser intensities (average of 130 evoked LFP responses from 13 mice). In this and the following figures, the peak amplitude was measured from baseline (dashed lines) to maximum negative peak amplitude. (*C*) Normalized increase in response peak amplitude (left) and decrease in response duration at half maximal amplitude (right) with increasing laser intensities ($n = 13$ mice). Responses were normalized and compared with control (no light; horizontal dashed lines). Paired t test, $^*P < 0.05$, $^{**}P < 0.01$ and $^{***}P < 0.001$). (*D1*) Fast Fourier transformation (FFT) of evoked LFP responses during no light (black line) and light on (gray line) conditions (average of 13 mice). Note the prominent increase of FFT power over a wide frequency band during optogenetic inactivation of PV interneurons. (*D2*) Bar diagram illustrating significant increase of FFT power during light pulse (Wilcoxon signed-rank test, $^{***}P < 0.001$).

increase of ~200% in peak MUA firing rate at 400 and 600 μm lateral and medial from the activated column (Fig. 5F). These MUA data and the spatial profile of the synaptic LFP responses indicate that PV-mediated disinhibition induces a widespread increase in synaptic excitation, but an increase in suprathreshold spiking activity only in neighboring columns. Next, we addressed the question over which intervals and at which time points the PV-mediated disinhibition exerts these strong network effects.

Temporal Profile of Transient PV-Mediated Disinhibition

In order to estimate the time window of disinhibition required for obtaining a significant effect on the synaptic LFP responses, single whisker stimulation was combined with laser pulses of increasing duration, starting 100 ms before the whisker stimulus (Fig. 6A). A 100 ms long laser pulse, which was terminated at the time point of whisker stimulation, had no effect on the evoked LFP response as compared with the whisker stimulation without light (0 ms trace in Fig. 6A), demonstrating that the ArchT-mediated hyperpolarization rapidly stopped when the laser was turned off. Gradually increasing the duration of the pulse to produce an overlap with the period of the LFP synaptic response had a significant effect at 15 ms poststimulus ($P < 0.05$, $n = 9$ mice; Fig. 6B). A further increase in response amplitude to 213 ± 32.8% could be observed at 20 ms overlap, when the disinhibition induced excitation reached a plateau. In agreement with the effects on the LFP peak amplitude and duration (Fig. 4C) these

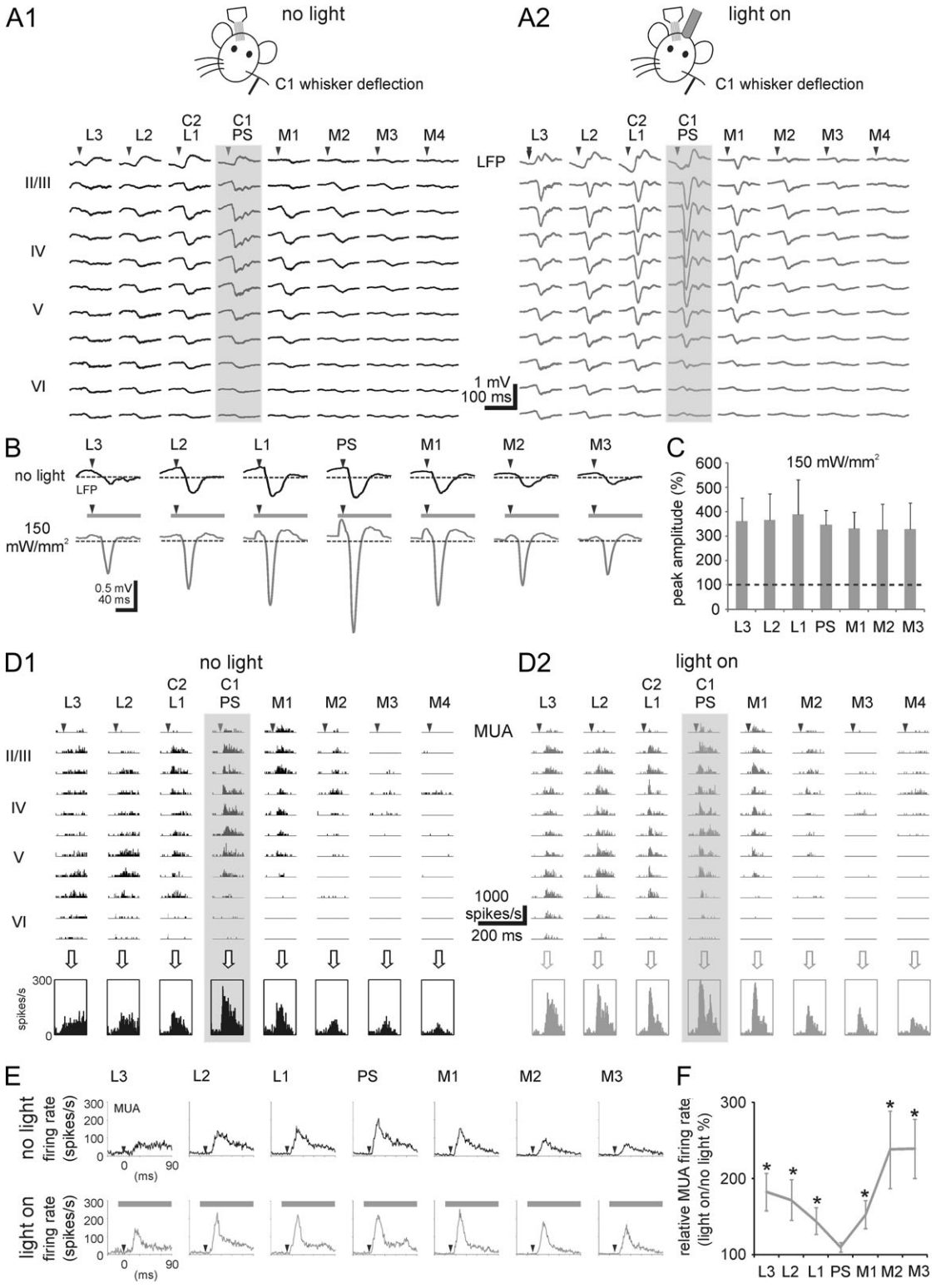

Figure 5. Optogenetic inactivation of PV interneurons causes a global increase in neocortical responses to single whisker stimulation. (*A*) Average LFP response to 10 stimulations of the C1 whisker under control conditions (A1, no light) and during optogenetic inactivation of PV interneurons (A2, light on). Note largest responses at principal shank (PS) located in the cortical column representing the C1 whisker. (*B*) Prominent increase in response amplitude (average of 80 evoked LFP responses from 8 mice) during optogenetic inactivation of PV inhibitory interneurons could be observed at all recording electrodes located up to 600 μm medial and lateral from the principal shank (PS). (*C*) Bar diagram illustrating that the increase in the response peak amplitude at lateral (L1–L3) and medial (M1–M3) shanks is not significantly different from that at principal shank (PS) ($n = 8$ mice). (*D*) Peristimulus time histograms (PSTHs) of MUA elicited by stimulation of whisker C1 under control conditions (no light, *D*1) and during optogenetic inactivation of PV inhibitory interneurons (light on, *D*2). Pooled MUAs recorded at different shanks are shown in lower row. (*E*) Average of pooled evoked MUAs recorded at the 7 different shanks under control conditions (upper panel, black) and during optogenetic disinhibition (lower panel, gray) ($n = 8$ mice). (*F*) The relative MUA firing rate was calculated by the ratio of mean MUA firing rate (light on/no light conditions) within ± 5 ms of maximum evoked MUA response. Note that response in principal column (PS) is not changed whereas MUA firing rate at neighboring recording sites is increased during disinhibition. (Paired *t* test, $^*P < 0.05$, $n = 8$ mice).

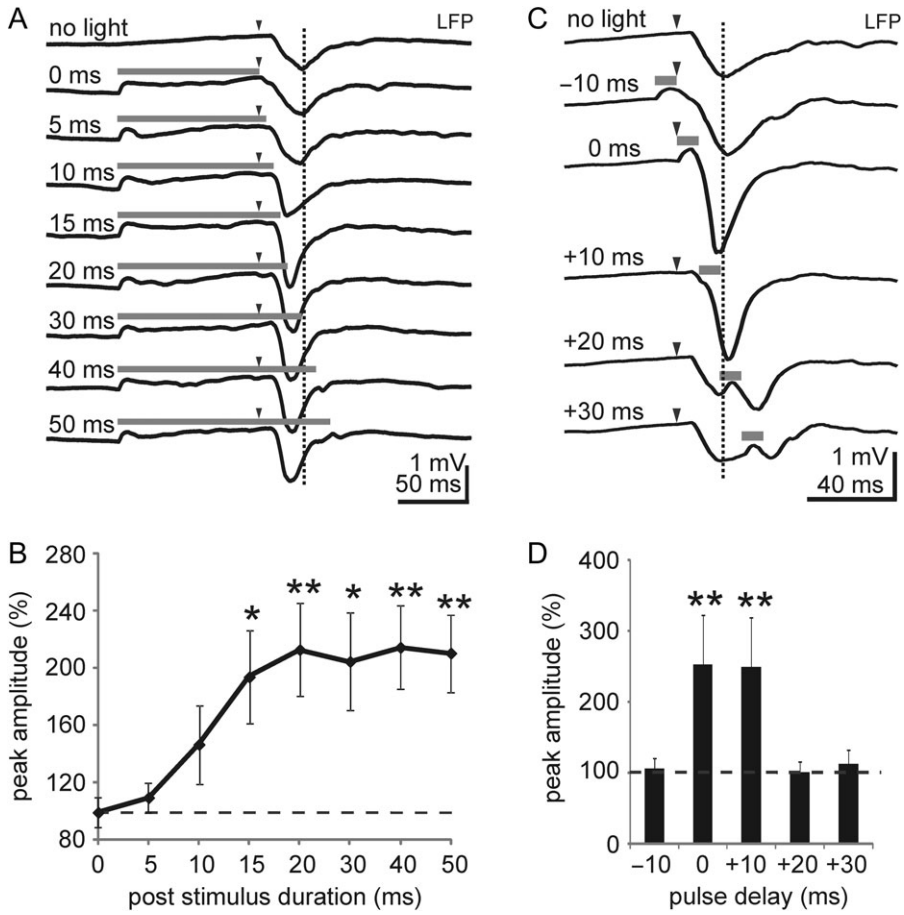

Figure 6. Effect of increasing disinhibition duration and influence of different timing of transient disinhibition on sensory-evoked cortical responses. (*A*) Average of 90 evoked LFP responses to single whisker stimulation combined with different durations of inhibiting PV interneurons ($n = 9$ mice). Note increase in response amplitude and decrease in delay of peak amplitude with increasing duration of optogenetic disinhibition, which starts 100 ms before whisker stimulation and ends 0–50 ms after the stimulus (gray horizontal lines). (*B*) Normalized peak amplitude of LFP response at increasing disinhibition intervals. (*C*) Timing of 10 ms disinhibition and effect on evoked LFP response (average of 80 evoked LFP responses from 8 mice). (*D*) Normalized first peak amplitude indicated by black dash line of LFP response at different disinhibition time points. Statistically significant differences (Wilcoxon signed-rank test) versus the control (no light) condition are indicated by *$P < 0.05$ and **$P < 0.01$.

data suggest that the PV-mediated disinhibition increases the network excitability already 15–20 ms poststimulus and a further prolongation in disinhibition does not have any stronger effect.

Since the ArchT kinetics are very fast, a 10 ms laser pulse was positioned at various time points before and after the whisker stimulus to further assess the temporal profile of the PV-mediated disinhibition (Fig. 6*C*, *D*). No effect on the LFP response could be observed when the pulse was applied 10 ms before the stimulus (–10 ms trace in Fig. 6*C*). When the pulse was applied during the first 10 ms poststimulus, the response peak amplitude increased significantly ($P < 0.01$) to 253.5 ± 69.3% (Fig. 6*C*, *D*). A similar response increase could be observed when the pulse was given during the second 10 ms interval poststimulus. At later intervals of > 20 ms, the peak amplitude in the LFP response was no longer influenced by a 10 ms disinhibition interval. These data indicate that the PV-mediated disinhibition has the most potent impact on cortical excitability during the first 20 ms after onset of the whisker stimulation.

Effect of Activation of PV Interneurons on Sensory-Evoked Response

We now investigated the impact of PV activation on single whisker-evoked responses in supragranular layers of the PS. For that, we expressed ChR2-mCherry in PV interneurons as described for ArchT experiments. Expression of ChR2 was again mainly constrained to layers II/III and V. The area of ChR2 expressing neurons constituted a cylinder with a diameter of 1335 ± 40 µm ($n = 5$ mice, Supplementary Fig. 9). For ChR2, we found a cell density of 3093 ± 399 cells/mm^3 in layer II/III, and 4297 ± 488 cells/mm^3 in layer V. In our functional experiments, opposite to inhibiting PV interneurons, we observed a prominent decrease in response amplitude upon illumination with 45 mW/mm^2 blue light (Fig. 7*A*). The decrease in response amplitude during activating PV interneurons was strongly dependent on the light intensity (Fig. 7*B*, *C*). Compared with the response under no light condition, already at a low intensity of 3.2 mW/mm^2 the peak amplitude was significantly decreased ($P < 0.001$, $n = 6$ mice) to 45.7 ± 4.8%. Higher intensities of 6.4, 22, 45, and 105 mW/mm^2 induced a further decrease of the peak amplitude, eventually abolishing most of the sensory-evoked response. This effect was accompanied by a significant decrease in the duration of the response at higher light intensity of 22, 45, and 105 mW/mm^2 (Fig. 7*C*).

Next, we studied the influence of transient PV activation on the spatial profile of evoked response. For that, we chose a low light intensity, which had shown to reduce but not completely abolish the evoked responses in the principal column. Notably,

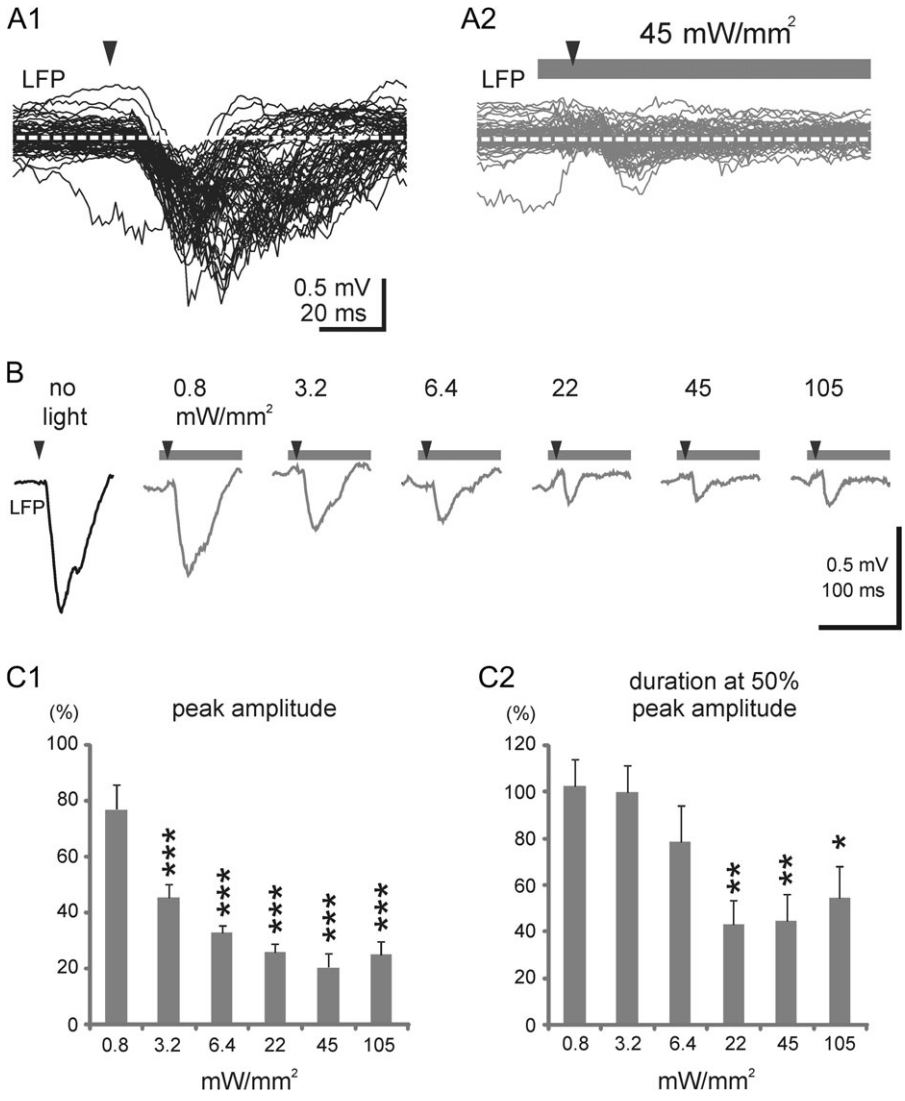

Figure 7. Optogenetic activation of PV interneurons causes amplitude decreases in stimulus-evoked cortical responses. (*A*) 60 superimposed raw traces ($n = 6$ animals) of evoked LFP activity recorded in deep layer II/III of the principal barrel column to single whisker stimulation under control condition (*A1*, no light) and during optogenetic activation of PV interneurons (*A2*, light on, 45 mW/mm^2). (*B*) Decrease of sensory-evoked response in layer II/III to increasing laser intensities (average of 60 evoked LFP responses from 6 mice). Note: the traces in *A2* and *B* with illumination were calculated by subtracting the LFP response during illumination without sensory stimulation from the sensory-evoked LFP response during the same intensity of illumination (see the details in Materials and Methods). (*C*) Normalized decrease in response peak amplitude (left) and decrease in response duration at half maximal amplitude (right) with increasing laser intensities ($n = 6$ mice). Responses were normalized and compared with control (no light). Paired *t* test, $^*P < 0.05$, $^{**}P < 0.01$, and $^{***}P < 0.001$).

illuminating the principal column with 3.2 mW/mm^2 light intensity induced a significant decrease of the LFP response peak amplitudes up to 600 µm lateral and medial of the PS (Fig. 8*A–C*). The evoked MUA activity, reflecting neuronal spiking, also decreased during the PV activation (Fig. 8*D–F*). These data indicate that the local and transient activation of PV interneurons induced a widespread excitability decrease, affecting several neighboring columns in barrel cortex.

We further studied the temporal profile of the impact of transiently activating PV interneurons on sensory-evoked responses. Differing from inhibiting PV interneurons (Fig. 6*A*, *B*), activating PV interneurons with a 100 ms laser pulse terminated directly prior to the onset of whisker stimulation already decreased the evoked LFP response (0 ms trace in Fig. 9*A*). Gradually increasing the duration of illumination—now overlapping with the whisker stimulus—did not further decrease the response amplitude (Fig. 9*B*). Applying short light pulses of 10 ms only effectively modulated sensory-evoked responses when applied either directly at or 10 ms after the onset of whisker stimulation (Fig. 9*C*, *D*). These data mirrors the temporal profile of PV-mediated disinhibition (Fig. 6*C*, *D*).

Next we were interested in the question, how many PV-expressing interneurons need to be modulated to have such prominent effects on cortical excitability.

A Small Number of Inhibited Interneurons Exert Significant Influence on the Cortical Representation of Sensory Stimuli

Estimating the number of effectively inhibited neurons in the local network requires 3 steps: (1) assessing the density of ArchT positive neurons, (2) estimating the photocurrent needed

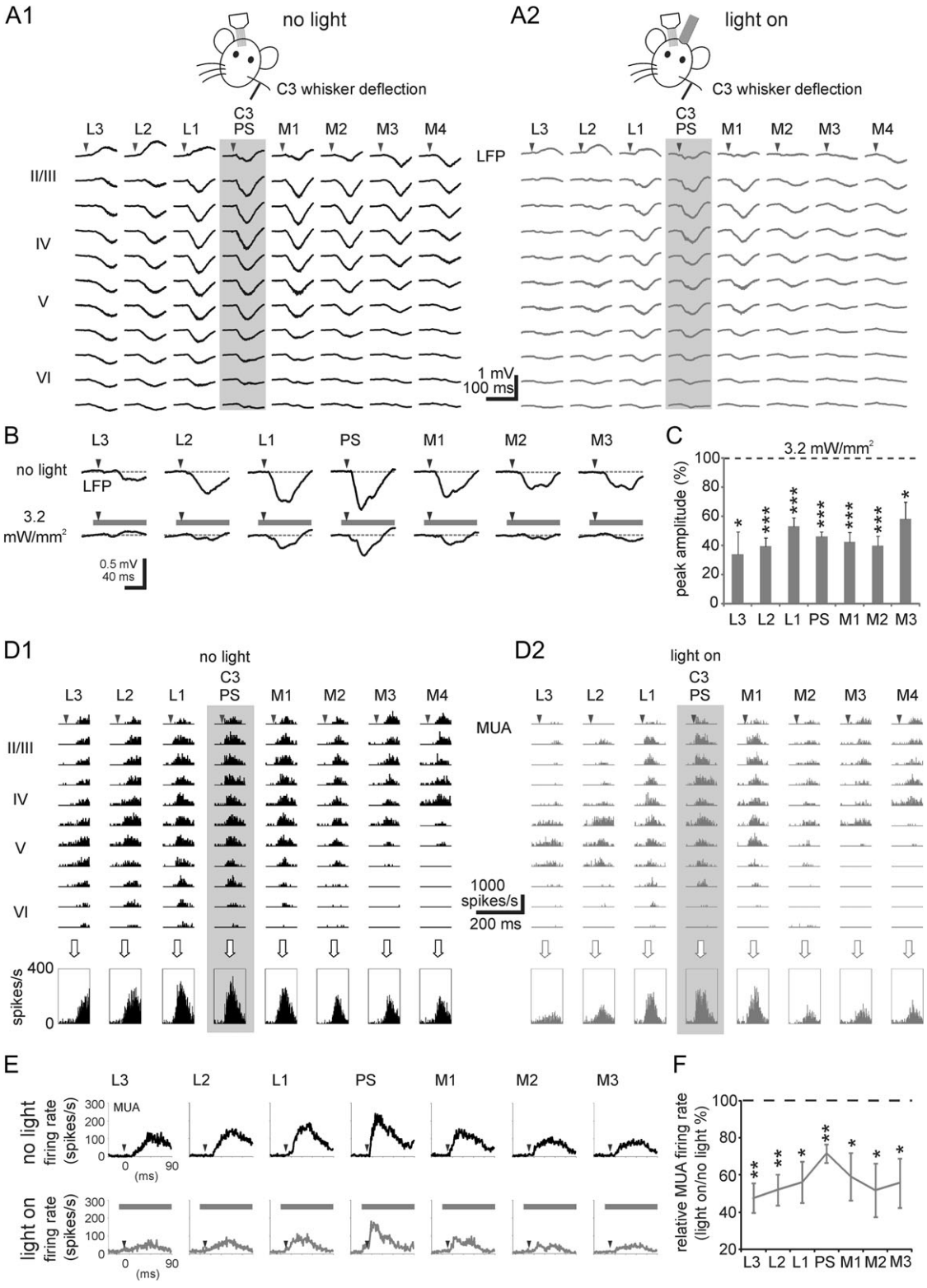

Figure 8. Optogenetic activation of PV interneurons lead to global decrease in neocortical responses to single whisker stimulation. (*A*) Average LFP response to 10 stimulations of the C3 whisker under control conditions (A1, no light) and during optogenetic activation of PV interneurons with an illumination density of 3.2 mW/mm^2 (A2, light on). (*B*) Prominent decrease in response amplitude (average of 60 evoked LFP responses from 6 mice) during optogenetic activation of PV interneurons could be observed at all recording electrodes located up to 600 μm medial and lateral from the principal shank (PS). (*C*) Bar diagram illustrating that the significant decrease of the LFP response peak amplitudes up to 600 μm lateral and medial of the PS (Paired t test, *$P < 0.05$ and ***$P < 0.001$, $n = 6$ mice). (*D*) Peri-stimulus time histograms (PSTHs) of MUA elicited by stimulation of whisker C3 under control conditions (no light, *D1*) and during optogenetic activation of PV interneurons (light on, *D2*). Pooled MUAs recorded at different shanks are shown in lower row. (*E*) Average of pooled evoked MUAs recorded at the 7 different shanks under control conditions (upper panel, black) and during optogenetic activation of PV interneurons (lower panel, gray) ($n = 6$ mice). (*F*) The relative MUA firing rate was calculated by the ratio of mean MUA firing rate (light on/no light conditions) within ± 5 ms of maximum evoked MUA response. There was a significant decrease of the MUA response up to 600 μm lateral and medial of the PS (paired *t* test, *$P < 0.05$ and **$P < 0.01$, $n = 6$ mice).

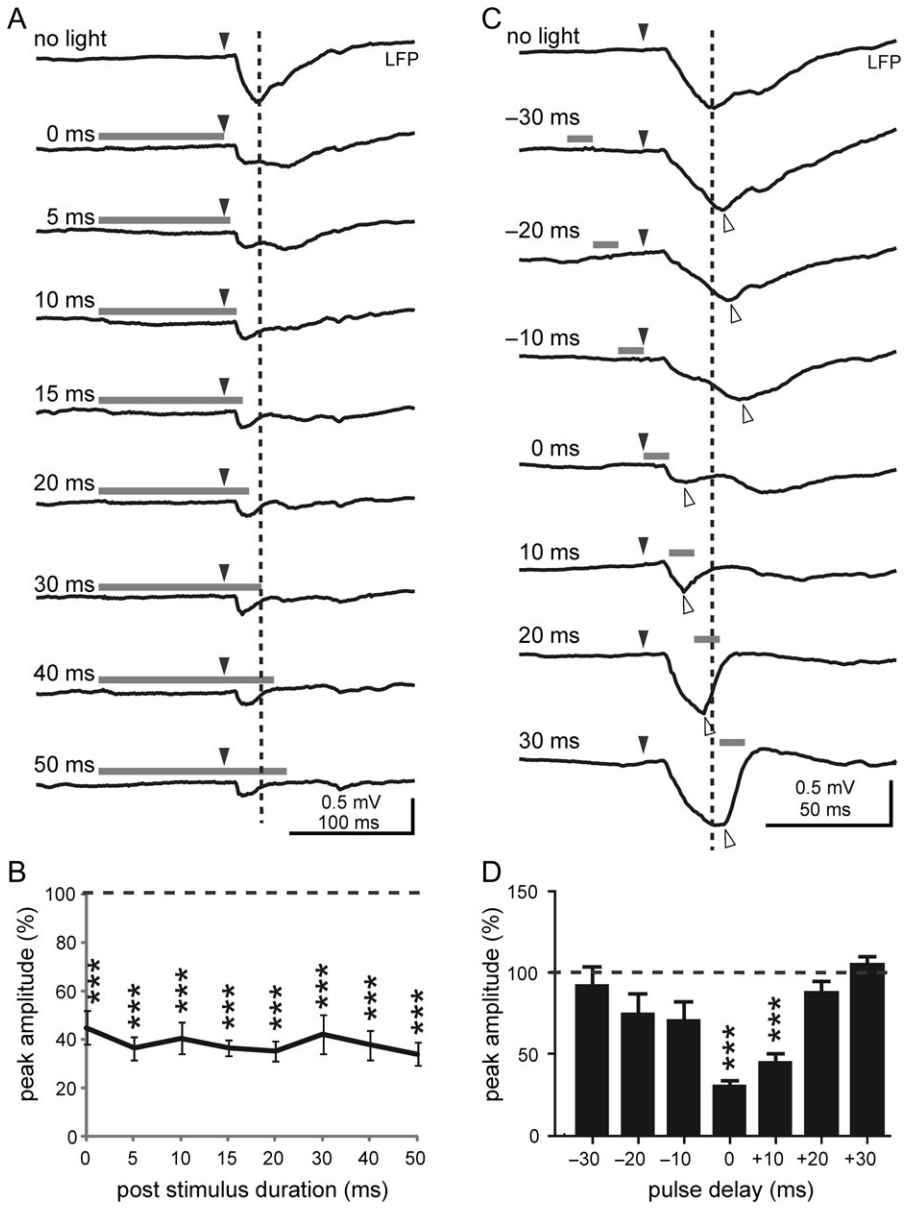

Figure 9. Effect of increasing PV-inhibition duration and influence of different timing of transient PV-inhibition on sensory-evoked cortical responses. (*A*) Average of 60 evoked LFP responses to single whisker stimulation combined with different durations of activating PV interneurons ($n = 6$ mice). (*B*) Normalized peak amplitude of LFP response at increasing PV-inhibition intervals. (*C*) Timing of 10 ms PV-inhibition and effect on evoked LFP response (average of 60 evoked LFP responses from 6 mice). (*D*) Normalized first peak amplitude indicated by empty arrows of LFP response at different PV-inhibition time points. Statistically significant differences (Paired *t* test) versus the control (no light) condition are indicated by ***$P < 0.001$.

for effective inhibition of action potential firing, and (3) estimating the light attenuation in tissue upon illumination with an optical fiber (Schmid et al. 2016). Firstly, the density of ArchT-tdTomato positive neurons in layer II/III and V was assessed in coronal brain slices using a dedicated epifluorescence microscope equipped with stereology software. We found that in layer II/III 2580 ± 250 cells/mm^3, and in layer V 2380 ± 890 cells/mm^3 ($n = 5$ mice) exhibit strong, membrane-bound expression of ArchT, about 2% of the neuronal population of the cortical column (78 986 ± 6046 neurons/mm^3, based on Lefort et al. 2009).

Given that 10–20% of the neuronal population are interneurons (based on Schüz and Palm 1989; Lefort et al. 2009; Gentet 2012), 10–20% of the interneuron population strongly express ArchT. Secondly, we assumed a minimal inhibitory current to be required for interneuron inhibition ranging at 200–250 pA (Galarreta and Hestrin 2002). To reach this current by ArchT activation, a local light density of > 1.5 mW/mm^2 is required (Han et al. 2011). Thirdly, we estimated the area in which the light density exceeds this threshold under our light delivery conditions using a 200 µm fiber with an NA of 0.39 and a light density of 150 mW/mm^2 at the tip of the fiber and a wavelength of 552 nm. The attenuation of light in brain tissue is dependent on species, wavelength, microarchitecture of the brain tissue, and vascularization. Implementing all these parameters in a comprehensive model has not been accomplished yet, the most common approach for modeling light attenuation is the Kubelka–Munk model, postulating a conical geometry (Aravanis et al. 2007).

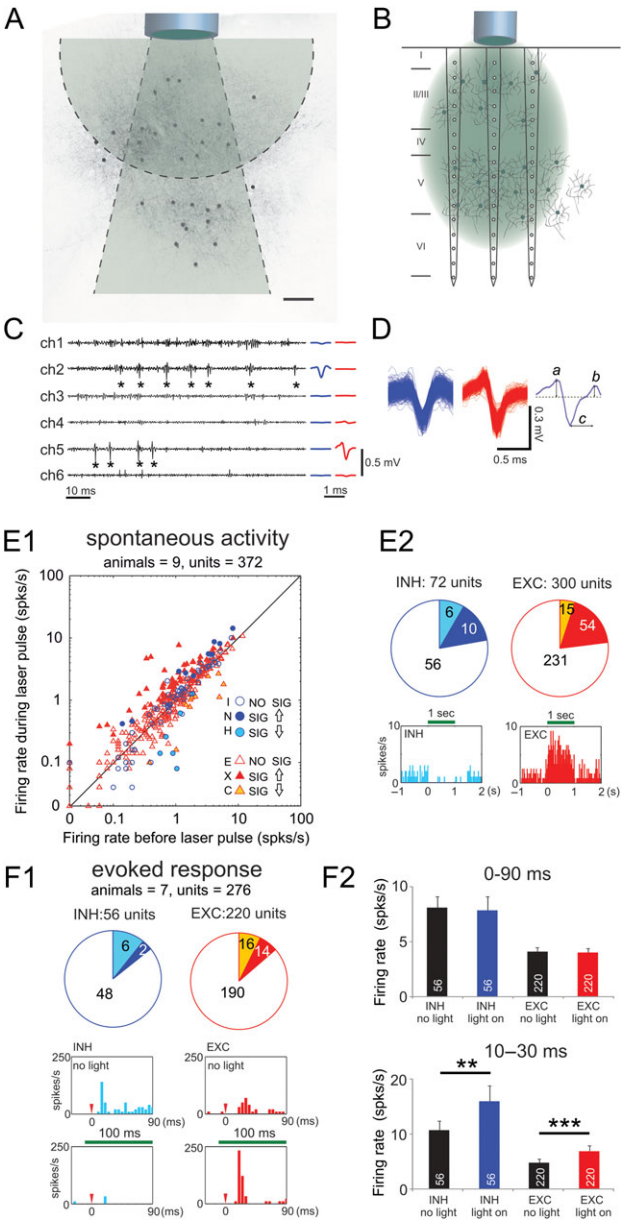

Figure 10. Optogenetic inactivation of a small number of PV interneurons exerts a global increase in neocortical activity. (*A*) Representation of light propagation relative to ArchT expression in mouse barrel cortex, overlaid with confocal micrograph of a coronal brain slice at the level of ArchT expression. Circle: representation of the spherical spread. Frustum: Representation of the Kubelka–Munk model. Scale bar: 100 µm. (*B*) Representation of average cell densities relative to the recording electrodes and cortex layers, overlaid with the area of above-threshold illumination based on a combination of modeling and experimental data. (*C*) High-pass filtered signals (0.8–5 kHz) from 6 channels recorded simultaneously with an 8-shank 128-channel probe showing single-unit spontaneous activity in a 100 ms long interval. Stars mark detected single unit events that were sorted as inhibitory (INH) and excitatory (EXC) neurons. Their average spike waveform profiles are shown in right panel (blue for INH and red for EXC). (*D*) Spike waveforms extracted from the INH and EXC neurons marked in C. The 3 features extracted from the spike waveforms to perform cell classification: *a* and *b*, early and late baseline-to-peak amplitude; *c*, trough to late peak latency (right panel). (*E1*) Comparing spontaneous mean firing rate of sorted units before versus during green light pulse (150 mW/mm^2). Circle symbols represent INHs and triangle symbols represent EXCs. Empty symbols represent neurons showing no significantly (NO SIG) different firing rates in both periods and filled symbols represent neurons showing significantly (SIG) different firing rates ($P < 0.05$, Wilcoxon signed-rank test). Dark and light blue circles represent INHs with significantly increasing (upward arrow) or decreasing firing rates (downward arrow), respectively. Red and yellow triangles represent EXCs with significantly increasing or decreasing firing rate, respectively. (*E2*) Pie charts showing the numbers of INHs and EXCs with no significantly different, significantly increasing and decreasing firing rates. Lower row shows examples of green light pulse inducing decrease in firing rate in 1 INH, and increase in firing rate in an EXC. (*F1*) Comparing evoked mean firing rate (0–90 ms after single whisker stimulation) of sorted units between no light versus green light pulse (150 mW/mm^2). Pie charts highlight the numbers of INHs and EXCs exhibiting significant increases or decreases (Mann–Whitney–Wilcoxon test). Examples of green light pulse decreasing evoked firing rate in 1 INH and increasing firing rate in another EXC. (*F2*) Upper panel shows the mean firing rate of INHs and EXCs in the time window of 90 ms after whisker deflection (number marked with bar diagram represent the number of units). Lower panel shows the mean firing rate of INHs and EXCs in the time window of 10–30 ms after whisker deflection. Note: data in *E* for spontaneous activity was in total 372 units from 9 mice and data in *F* for evoked response was in total 276 units from 7 mice.

However, existing experimental data strongly suggest that this model underestimates lateral scattering proximal to the fiber tip (Yizhar et al. 2011; Stroh et al. 2013). This deviation from the conical model is less prominent for deeper structures, therefore, for layer V we used only the Kubelka–Munk model, for layers II/III we considered a spherical model in addition, representing an extreme scenario of lateral scattering (Fig. 10A) (Schmid et al. 2016).

The fiber being placed on top of the cortical surface, using the Kubelka–Munk model and applying a power density of 150 mW/mm^2 at the fiber tip, the inhibition threshold of 1.5 mW/mm^2 is reached at a distance of 0.8 mm, exceeding the extent of expression in dorsoventral direction. For the lateral extent, assuming the extreme case of the spherical model, the entire layer II/III expressing region would be within above-threshold illumination (Fig. 10A). Taken together with the cell density measures, 250 ± 24 (n = 5 mice) PV positive interneurons were inhibited in layer II/III according to the spherical model. Assuming the Kubelka–Munk model, in layer II/III, a volume of 0.0376 mm^3 would be illuminated, smaller than the volume of expression, resulting in 97 ± 10 inhibited neurons. In layer V, due to the conical spread assumed by the model, the entire expression is illuminated above threshold, thus 162 ± 18 neurons are estimated to be affected under our illumination conditions. Therefore we conclude, that a typical light pulse optogenetically inhibits between 260 and 410 cells, covering 3 electrode shanks, assuming an ellipsoid shape (Fig. 10B) based on model and experimental data (Yizhar et al. 2011). In the case of ChR2 stimulation, using similar volume calculations (see Materials and Methods for detail), resulted in 74 ± 9 to 116 ± 14 cells in layer II/III depending on the model of light propagation and 67 ± 8 cells in layer V. In total between 140 and 180 cells were excited in these experiments.

To relate these cell numbers to functional data in our experimental setting, we conducted a single-unit analysis of the MEA data for the ArchT mediated disinhibition. This method allowed the simultaneous recording of numerous single units, which were classified as putative INH and EXC neurons (Fig. 10C, D, Supplementary Fig. 10; for details see Reyes-Puerta, Kim et al. 2015; Reyes-Puerta, Sun et al. 2015). In total, 526 single units were detected (n = 13 mice), 79% (415) of these units were identified as EXC neurons, 21% (111) were identified as INH neurons (Supplementary Fig. 10), in line with the aforementioned histology data. The putative inhibitory neurons include both PV and SOM cells (Ascoli et al. 2008; Rudy et al. 2011), but is not limited to them. In this regard, all subtypes of fusiform neocortical interneurons have shorter spike duration than pyramidal cells (Cauli et al. 2000).

In the lateral amygdala, cluster analysis of interneurons identified only one major subtype (burst-firing adapting, ~15% of the total population of GABAergic cells) which present broad spikes comparable to pyramidal cells (Sosulina et al. 2010). Taking into account all these studies, we estimate that in our data the sorted putative interneurons represent not only PV and SOM cells, but also other interneuron types with narrow spike waveforms, thus accounting for >80% of the total population of inhibitory cells. A small proportion of GABAergic neurons were possibly misclassified as putative EXC neurons—but this accounts for <5% of the total population of EXC cells, due to the larger size of this group.

Upon illumination during spontaneous activity recordings (n = 10 mice), 8.3% (6 of 72 INH units) of the putative INH neurons significantly decreased their firing rate (Fig. 10*E*), well matching our histological quantifications given the variability of the parameters involved. Notably, 10 inhibitory neurons increased their firing activity, yet it has to be noted, that our recordings cannot differentiate between PV and other interneurons, and secondary network effects may occur. While about 18% of excitatory neurons exhibited a significant increase, 5% showed a decrease in firing rate. Studying the single unit responses after whisker stimulation during illumination, about 11% of the inhibitory neurons (6 of 56 INH units) significantly decreased their firing rate (Fig. 10*F*), very similar compared with spontaneous activity, and a small proportion of 4% increased firing activity. The excitatory units exhibited an equal proportion of significantly increased and decreased firing rate (6% increase, 7% decrease). Interestingly, averaging the firing rate in the time window of 90 ms after whisker deflection resulted in no effect on both excitatory and inhibitory firing rate. However, when limiting the analysis to a 20 ms time window, covering the peak response (Fig. 6*B*, *D*), we notably detected a significant increase of excitatory and inhibitory firing rate (P = 0.0002 for EXC, P = 0.0072 for INH) (Fig. 10*F*2).

In summary, our results indicate that modifying locally a very small subset of PV interneurons exerts a prominent global effect on excitatory and inhibitory neurons, both during spontaneous as well as stimulus-evoked activity, and that this effect exhibits a high degree of temporal specificity.

Discussion

In the present study, we found that inhibiting PV interneurons causes a broad spectrum increase of spontaneous activity in mouse barrel cortex in vivo. Oppositely, activating PV interneurons strongly reduced the power spectrum of spontaneous activity. Furthermore, PV-mediated disinhibition upon single whisker stimulation induces a widespread increase in synaptic excitation, but an increase in suprathreshold spiking activity only in neighboring columns. In contrast, activating PV interneurons decreased synaptic excitation and spiking activity both in principal and neighboring barrel columns. These effects are short-lasting and are critically dependent on the timing of optogenetic modulation, with the strongest impact on cortical excitability during the first 20 ms after onset of whisker stimulation. Notably, this drastic effect is mediated by a rather small number of PV interneurons, constituting only around 10% of the local PV population, ranging at a few hundred neurons.

Implementing an Optogenetic Approach to Silence or Activate Interneurons in Combination With MEA Recordings

One of the inherent pitfalls of genetic targeting of opsin expression to a defined neuronal subpopulation is the specificity of the promoter. This is of particular relevance for approaches employing a direct control of opsin expression by a cell-type specific promoter encoded in 1 viral plasmid. In this case, 2 conditions have to be met: firstly, the expression needs to be rendered specific, and secondly, a high expression level has to be realized, as the photocurrent brought about by individual pumps is rather small and therefore a large number of opsins need to be expressed (Sohal et al. 2009; Fois et al. 2014). Typically, promoters specific for interneuron populations are rather weak, so a direct control of ArchT or ChR2 expression by the PV promoter will not lead to sufficient opsin expression. Here, we circumvent this problem by employing a transgenic mouse expressing the enzyme cre-recombinase in PV interneurons only (Sohal et al. 2009). Upon injection of a viral construct driving expression of ArchT or ChR2 by a strong ubiquitous promoter but flanked by 2 flox cassettes, expression will be limited to cre-expressing interneurons, but at the same time driven by a strong promoter (Cardin et al. 2009). However, we still could not confirm that 100% of the expressing cells are PV-positive. Indeed, while PV is exclusively expressed by GABAergic interneurons and mainly by the so called basket cell class, it is also expressed at lower levels by other types of interneurons (Gentet 2012). Our results are well in line with these reports, as we could indeed rule out expression in excitatory neurons.

Assessing the Scope of Optogenetic Network Modulation

Multiple experimental parameters influence the scope of optogenetic network activation: Firstly, AA-virus injections inherently result in varying infection rates per neuron due to multiplicity of infection, leading to heterogeneity of opsin expression (Aschauer et al. 2013), this in turn affecting inhibitory photocurrents. However, while this induces jitter, it might create a less artificial pattern of inhibition. Secondly, while light penetration can be estimated by established models, the highly heterogeneous brain tissue, in particular the high-light scattering and absorbent microvasculature, can only be modeled to a certain extent. Finally, for optical inhibition even more so than for excitation, efficient inhibition of action potential firing depends on many physiological parameters like neuromodulation, state of the animal, membrane resistance, and synaptic inputs (Lee et al. 2014). This inherently limits the accuracy of any approach assessing the scope of optogenetic network modulation.

While initial studies employed the Kubelka–Munk model (Aravanis et al. 2007), assuming a conical spread, experimental data revealed that this approach underestimates the lateral spread (Yizhar et al. 2011; Stroh et al. 2013). More complex modeling approaches based on Monte Carlo simulations led to rather ellipsoid geometries (Yizhar et al. 2011; Yona et al. 2016). In our present study, the correlation of histology/modeling data using the combination of 2 geometrical models with actual single unit recordings resulted in a striking convergence of optogenetically modulated cell numbers, mutually supporting the validity of our estimates.

Impact on Power Spectra of Spontaneous and Evoked Activity

We found that transient inhibition of a small number of PV interneurons causes a significant broad spectrum increase both in spontaneous and evoked network activity, ranging from theta to

gamma frequency bands (Figs 3 and 4). Activation of PV interneurons during spontaneous activity significantly reduces spectral LFP power over wide range of frequencies (Suppl. Fig. 4). An earlier study in the prefrontal cortex found that optogenetic inhibition of PV interneurons reduces power in the gamma frequency band evoked by light activation of excitatory pyramidal neurons (Sohal et al. 2009). Different experimental designs between this earlier study and our present work may explain this discrepancy. Firstly, rodent prefrontal and barrel cortex exhibit prominent differences in cytoarchitecture, with the prefrontal cortex being largely devoid of granular layer IV (Shepherd 2009; Van De Werd et al. 2010). Secondly, Sohal et al. optically activated ChR2-expressing excitatory neurons, while here we deflected single whiskers, directly activating both excitatory and inhibitory neural networks in barrel cortex. In the visual cortex of the mouse, lacking layer IV barrels but exhibiting a similar organization of horizontal layers, the optogenetic inhibition of PV interneurons led to an increase in the spiking rate of pyramidal cells (Atallah et al. 2012), in agreement to our data. It has to be noted, that LFP and MUA represent qualitatively different readouts of neuronal activity. LFP majorly reflects the subthreshold membrane potential changes of a rather large population of neurons surrounding the recording site, potentially still being impacted by activity from more than 1 cm from its origin (Kajikawa and Schroeder 2011). Conversely, MUA reveals the suprathreshold activation of neurons within a radius of only about 140 μm from the recording site (Buzsáki 2004). Consequently, when placed in the PS, only MUA recordings will be able to unambiguously reflect activity within this shank, while LFP, which also dominated by local activity, will also be impacted by activity outside of the PS, and integrate nonlinearly both spiking and synaptic activity (Buzsáki et al. 2012). Therefore, local spiking specific readouts are better suitable assessing the lateral spread of evoked cortical activity.

Impact of PV Modulation on Slow Oscillations

During quiet wakefulness, NREM sleep and some forms of anesthesia (e.g., urethane or ketamine-xylazine), cortical dynamics show prominent slow oscillations (~1 Hz Up and Down states) (Steriade et al. 1993; Stroh et al. 2013; Fiáth et al. 2016; Reyes-Puerta et al. 2016). In the present study we indeed observed spontaneous Up–Down state transitions. We demonstrated that under urethane anesthesia, inhibiting PV interneurons reliably induced transitions form Down to Up states and extended the duration of Up state accompanied with an increase in high frequency oscillations nested within Up state, as previously proposed by Compte et al. (2008). In contrast, activating PV interneurons reduced the occurrence of slow oscillation as well as the high frequency oscillations occurring during an Up state. These results are well in line with a recent study showing that PV interneurons play a role in modulating the slow oscillation (Zucca et al. 2017). Note, that activating PV interneurons did not completely abolish the occurrence of up states. Indeed, it has been shown that modulating SST interneurons (Zucca et al. 2017) and excitatory neurons (Stroh et al. 2013) also impact Up–Down state transitions. In the future, it will be interesting to perform optogenetic modulation of all relevant cortical cell types to explore their specific role in those state transitions.

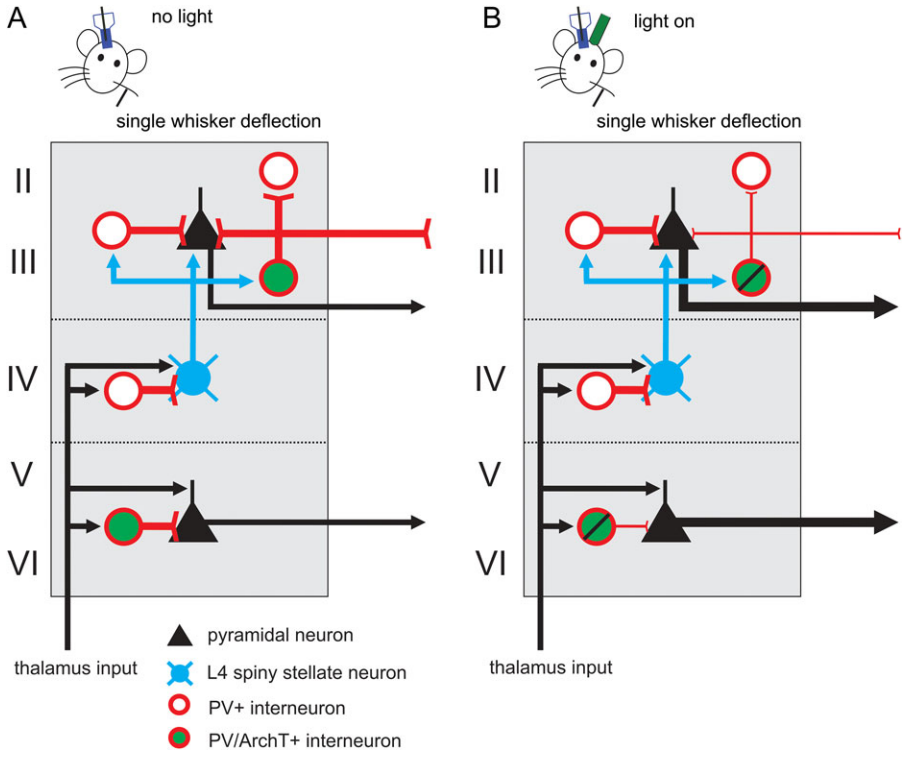

Figure 11. The influence of the PV-mediated disinhibition on the signal processing of evoked response by single whisker stimulation. (A) Under normal condition, the evoked information by single whisker stimulation is transferred by thalamus into corresponding principal barrel column. The thalamic input targets layer IV spiny stellate neurons (blue), PV+ interneurons (red circle) and deep layer pyramidal neurons (black triangle). PV+ interneurons provide feedforward and lateral inhibition on pyramidal neurons and other PV+ interneurons. In this study, the ArchT/PV+ interneurons (red circle filled with green color) are located in layer II/III and deep layers. (B) During optogenetic inhibition of ArchT/PV+ interneurons, the output strength of PV/ArchT+ interneurons decreases and the output strength of pyramidal neurons in layer II/III and deep layers to neighboring columns increases.

Impact on Spatiotemporal Representation of Sensory-Evoked Activity

Each PV+ interneuron innervates 200–1000 pyramidal neurons, thereby controlling the synchrony of cortical network activity (Kubota 2014). However, PV+ interneurons not only target pyramidal cells, but also connect to each other by electrical synapses and by reciprocal GABAergic chemical synapses (Galarreta and Hestrin 1999, 2002; Gibson et al. 1999). In addition, a high degree of connectivity between PV+ and somatostatin-expressing (SOM+) interneurons by inhibitory chemical synapses has been reported (Gibson et al. 1999). Along this line, here we did not only observe an optogenetically modulated reduction, but also an increase of interneuron activity, suggesting secondary network effects.

In vitro experimental evidence demonstrates a small, functionally defined subpopulation of fast-spiking neurons in layer IV, which mediates thalamocortical feedforward inhibition in excitatory neurons, therefore directly affecting spiking output of the excitatory network in barrel cortex (Sun et al. 2006). This powerful feedforward inhibition, presumably provided by PV+ interneurons, shortens the coincidence detection window in pyramidal neurons (Pouille and Scanziani 2001). Our data shows that inhibiting a small number of PV+ interneurons in layers II/III and V impacts cortical excitability most strongly during the first 20 ms after onset of whisker stimulation, supporting the "window of opportunity" concept (Pritchett et al. 2015).

Besides feedforward inhibition, PV+ interneurons also have been proposed to play an important role in controlling lateral inhibition. Chagnac-Amitai and Connors (1989) reported that a 10–20% reduction in GABAergic inhibition causes a prominent increase in the horizontal spread of excitation. Anatomical evidence in rat barrel cortex shows large basket interneurons, presumably PV interneurons in layer II/II, extend their terminals several hundred micrometers away (Helmstaedter et al. 2009), allowing long-range lateral inhibition. Indeed, we found that inhibiting a small portion of PV interneurons causes a widespread increase of sensory-evoked LFP response reaching at least 1.2 mm in diameter from the principal column, which correlated with the stronger increase in spiking activity in neighboring columns. These results confirm the important role of PV interneurons in cortical lateral inhibition.

Strikingly, in multiunit recordings, representing spatially well-defined neuronal firing rates, no change was observed in the PS, situated well within the transfected barrel, but an increase of MUA was observed at 200–600 μm laterally in each direction. Moreover, within the PS, no measureable effect on neuronal spiking was found even in the very layers exhibiting robust expression of ArchT (Fig. 5F, Supplementary Fig. 8). This supports the notion of PV+ interneurons playing a highly specific role in cross-columnar (as opposed to intracolumnar) inhibition (Fig. 11).

Authors' Contributions

Conceived and designed the experiments: M.C.S., A.S., H.J.L. Performed the experiments: J.W.Y., P.H.P. Analyzed the data: J.W.Y., P.H.P., V.R.P., A.S. Wrote the article: M.C.S., A.S., H.J.L.

Supplementary Material

Supplementary data are available at *Cerebral Cortex* online.

Funding

DFG grants LU 375/11-1 (H.J.L.) and STU 544/3-1 (M.C.S.), CRC 1080, SPP 1665 (A.S.), the FTN, and the DFG major equipment (A.S.).

Notes

We would like to thank Michaela Moisch and Beate Krumm for excellent technical assistance. *Conflict of Interest*: None declared.

References

Aravanis AM, Wang L-P, Zhang F, Meltzer LA, Mogri MZ, Schneider MB, Deisseroth K. 2007. An optical neural interface: in vivo control of rodent motor cortex with integrated fiberoptic and optogenetic technology. J Neural Eng. 4: S143–S156.

Aschauer DF, Kreuz S, Rumpel S. 2013. Analysis of transduction efficiency, tropism and axonal transport of AAV serotypes 1, 2, 5, 6, 8 and 9 in the mouse brain. PLoS One. 8:e76310.

Ascoli GA, Alonso-Nanclares L, Anderson SA, Barrionuevo G, Benavides-Piccione R, Burkhalter A, Buzsáki G, Cauli B, Defelipe J, Fairén A, et al. 2008. Petilla terminology: nomenclature of features of GABAergic interneurons of the cerebral cortex. Nat Rev Neurosci. 9:557–568.

Atallah BV, Bruns W, Carandini M, Scanziani M. 2012. Parvalbumin-expressing interneurons linearly transform cortical responses to visual stimuli. Neuron. 73:159–170.

Berndt A, Deisseroth K. 2015. OPTOGENETICS. Expanding the optogenetics toolkit. Science. 349:590–591.

Boyden ES, Zhang F, Bamberg E, Nagel G, Deisseroth K. 2005. Millisecond-timescale, genetically targeted optical control of neural activity. Nat Neurosci. 8:1263–1268.

Buzsáki G. 2004. Large-scale recording of neuronal ensembles. Nat Neurosci. 7:446–451.

Buzsáki G, Anastassiou CA, Koch C. 2012. The origin of extracellular fields and currents—EEG, ECoG, LFP and spikes. Nat Rev Neurosci. 13:407–420.

Cardin JA, Carlén M, Meletis K, Knoblich U, Zhang F, Deisseroth K, Tsai L-H, Moore CI. 2009. Driving fast-spiking cells induces gamma rhythm and controls sensory responses. Nature. 459:663–667.

Cardin JA, Carlén M, Meletis K, Knoblich U, Zhang F, Deisseroth K, Tsai L-H, Moore CI. 2010. Targeted optogenetic stimulation and recording of neurons in vivo using cell-type-specific expression of Channelrhodopsin-2. Nat Protoc. 5:247–254.

Cauli B, Porter JT, Tsuzuki K, Lambolez B, Rossier J, Quenet B, Audinat E. 2000. Classification of fusiform neocortical interneurons based on unsupervised clustering. Proc Natl Acad Sci USA. 97:6144–6149.

Chagnac-Amitai Y, Connors BW. 1989. Horizontal spread of synchronized activity in neocortex and its control by GABA-mediated inhibition. J Neurophysiol. 61:747–758.

Compte A, Reig R, Descalzo VF, Harvey MA, Puccini GD, Sanchez-Vives MV. 2008. Spontaneous high-frequency (10-80 Hz) oscillations during up states in the cerebral cortex in vitro. J Neurosci. 28:13828–13844.

Deisseroth K. 2015. Optogenetics: 10 years of microbial opsins in neuroscience. Nat Neurosci. 18:1213–1225.

Fiáth R, Kerekes BP, Wittner L, Tóth K, Beregszászi P, Horváth D, Ulbert I. 2016. Laminar analysis of the slow wave activity in the somatosensory cortex of anesthetized rats. Eur J Neurosci. 44:1935–1951.

Fois C, Prouvot P-H, Stroh A. 2014. A roadmap to applying optogenetics in neuroscience. Methods Mol Biol. 1148:129–147.

Freeman JA, Nicholson C. 1975. Experimental optimization of current source-density technique for anuran cerebellum. J Neurophysiol. 38:369–382.

Galarreta M, Hestrin S. 1999. A network of fast-spiking cells in the neocortex connected by electrical synapses. Nature. 402:72–75.

Galarreta M, Hestrin S. 2002. Electrical and chemical synapses among parvalbumin fast-spiking GABAergic interneurons in adult mouse neocortex. Proc Natl Acad Sci USA. 99: 12438–12443.

Gentet LJ. 2012. Functional diversity of supragranular GABAergic neurons in the barrel cortex. Front Neural Circuits. 6:52.

Gibson JR, Beierlein M, Connors BW. 1999. Two networks of electrically coupled inhibitory neurons in neocortex. Nature. 402:75–79.

Govorunova EG, Sineshchekov OA, Janz R, Liu X, Spudich JL. 2015. Natural light-gated anion channels: a family of microbial rhodopsins for advanced optogenetics. Science. 349 (6248):647–650.

Han X, Chow BY, Zhou H, Klapoetke NC, Chuong A, Rajimehr R, Yang A, Baratta MV, Winkle J, Desimone R, et al. 2011. A high-light sensitivity optical neural silencer: development and application to optogenetic control of non-human primate cortex. Front Syst Neurosci. 5:18.

Harris KD, Henze DA, Csicsvari J, Hirase H, Buzsáki G. 2000. Accuracy of tetrode spike separation as determined by simultaneous intracellular and extracellular measurements. J Neurophysiol. 84:401–414.

Hazan L, Zugaro M, Buzsáki G. 2006. Klusters, NeuroScope, NDManager: a free software suite for neurophysiological data processing and visualization. J Neurosci Methods. 155: 207–216.

Helmstaedter M, Sakmann B, Feldmeyer D. 2009. Neuronal correlates of local, lateral, and translaminar inhibition with reference to cortical columns. Cereb Cortex. 19:926–937.

Huber D, Petreanu L, Ghitani N, Ranade S, Hromádka T, Mainen Z, Svoboda K. 2008. Sparse optical microstimulation in barrel cortex drives learned behaviour in freely moving mice. Nature. 451:61–64.

Kajikawa Y, Schroeder CE. 2011. How local is the local field potential? Neuron. 72:847–858.

Kätzel D, Zemelman BV, Buetfering C, Wölfel M, Miesenböck G. 2011. The columnar and laminar organization of inhibitory connections to neocortical excitatory cells. Nat Neurosci. 14: 100–107.

Krupa DJ, Brisben AJ, Nicolelis MA. 2001. A multi-channel whisker stimulator for producing spatiotemporally complex tactile stimuli. J Neurosci Methods. 104:199–208.

Kubota Y. 2014. Untangling GABAergic wiring in the cortical microcircuit. Curr Opin Neurobiol. 26:7–14.

Laxpati NG, Mahmoudi B, Gutekunst C-A, Newman JP, Zeller-Townson R, Gross RE. 2014. Real-time in vivo optogenetic neuromodulation and multielectrode electrophysiologic recording with NeuroRighter. Front Neuroeng. 7:40.

Lee AM, Hoy JL, Bonci A, Wilbrecht L, Stryker MP, Niell CM. 2014. Identification of a brainstem circuit regulating visual cortical state in parallel with locomotion. Neuron. 83: 455–466.

Lefort S, Tomm C, Floyd Sarria J-C, Petersen CCH. 2009. The excitatory neuronal network of the C2 barrel column in mouse primary somatosensory cortex. Neuron. 61:301–316.

Li L-Y, Xiong XR, Ibrahim LA, Yuan W, Tao HW, Zhang LI. 2015. Differential receptive field properties of parvalbumin and somatostatin inhibitory neurons in mouse auditory cortex. Cereb Cortex. 25:1782–1791.

Li L, Ji X, Liang F, Li Y, Xiao Z, Tao HW, Zhang LI. 2014. A feed-forward inhibitory circuit mediates lateral refinement of sensory representation in upper layer 2/3 of mouse primary auditory cortex. J Neurosci. 34:13670–13683.

Meyer HS, Schwarz D, Wimmer VC, Schmitt AC, Kerr JND, Sakmann B, Helmstaedter M. 2011. Inhibitory interneurons in a cortical column form hot zones of inhibition in layers 2 and 5A. Proc Natl Acad Sci USA. 108:16807–16812.

Pouchelon G, Gambino F, Bellone C, Telley L, Vitali I, Lüscher C, Holtmaat A, Jabaudon D. 2014. Modality-specific thalamocortical inputs instruct the identity of postsynaptic L4 neurons. Nature. 511:471–474.

Pouille F, Scanziani M. 2001. Enforcement of temporal fidelity in pyramidal cells by somatic feed-forward inhibition. Science. 293:1159–1163.

Prigge M, Schneider F, Tsunoda SP, Shilyansky C, Wietek J, Deisseroth K, Hegemann P. 2012. Color-tuned channelrhodopsins for multiwavelength optogenetics. J Biol Chem. 287: 31804–31812.

Pritchett DL, Siegle JH, Deister CA, Moore CI. 2015. For things needing your attention: the role of neocortical gamma in sensory perception. Curr Opin Neurobiol. 31:254–263.

Reyes-Puerta V, Kim S, Sun J-J, Imbrosci B, Kilb W, Luhmann HJ. 2015. High stimulus-related information in barrel cortex inhibitory interneurons. PLoS Comput Biol. 11:e1004121.

Reyes-Puerta V, Sun J-J, Kim S, Kilb W, Luhmann HJ. 2015. Laminar and columnar structure of sensory-evoked multineuronal spike sequences in adult rat barrel cortex in vivo. Cereb Cortex. 25:2001–2021.

Reyes-Puerta V, Yang J-W, Siwek ME, Kilb W, Sun J-J, Luhmann HJ. 2016. Propagation of spontaneous slow-wave activity across columns and layers of the adult rat barrel cortex in vivo. Brain Struct Funct. 221(9):4429–4449.

Rudy B, Fishell G, Lee S, Hjerling-Leffler J. 2011. Three groups of interneurons account for nearly 100% of neocortical GABAergic neurons. Dev Neurobiol. 71:45–61.

Sachidhanandam S, Sermet BS, Petersen CCH. 2016. Parvalbumin-expressing GABAergic neurons in mouse barrel cortex contribute to gating a goal-directed sensorimotor transformation. Cell Rep. 15:700–706.

Schiffman HR, Lore R, Passafiume J, Neeb R. 1970. Role of vibrissae for depth perception in the rat (*Rattus norvegicus*). Anim Behav. 18:290–292.

Schmid F, Wachsmuth L, Schwalm M, Prouvot P-H, Jubal ER, Fois C, Pramanik G, Zimmer C, Faber C, Stroh A. 2016. Assessing sensory versus optogenetic network activation by combining (o)fMRI with optical Ca^{2+} recordings. J Cereb Blood Flow Metab. 36(11):1885–1900.

Schüz A, Palm G. 1989. Density of neurons and synapses in the cerebral cortex of the mouse. J Comp Neurol. 286:442–455.

Schwaller B, Tetko IV, Tandon P, Silveira DC, Vreugdenhil M, Henzi T, Potier M-C, Celio MR, Villa AEP. 2004. Parvalbumin deficiency affects network properties resulting in increased susceptibility to epileptic seizures. Mol Cell Neurosci. 25:650–663.

Shepherd GMG. 2009. Intracortical cartography in an agranular area. Front Neurosci. 3:337–343.

Sohal VS, Zhang F, Yizhar O, Deisseroth K. 2009. Parvalbumin neurons and gamma rhythms enhance cortical circuit performance. Nature. 459:698–702.

Sosulina L, Graebenitz S, Pape H-C. 2010. GABAergic interneurons in the mouse lateral amygdala: a classification study. J Neurophysiol. 104:617–626.

Steriade M, Nuñez A, Amzica F. 1993. A novel slow (<1 Hz) oscillation of neocortical neurons in vivo: depolarizing and hyperpolarizing components. J Neurosci. 13:3252–3265.

Stroh A, Adelsberger H, Groh A, Rühlmann C, Fischer S, Schierloh A, Deisseroth K, Konnerth A. 2013. Making waves: initiation and propagation of corticothalamic Ca^{2+} waves in vivo. Neuron. 77:1136–1150.

Sun Q-Q, Huguenard JR, Prince DA. 2006. Barrel cortex microcircuits: thalamocortical feedforward inhibition in spiny stellate cells is mediated by a small number of fast-spiking interneurons. J Neurosci. 26:1219–1230.

Van De Werd HJJM, Rajkowska G, Evers P, Uylings HBM. 2010. Cytoarchitectonic and chemoarchitectonic characterization of the prefrontal cortical areas in the mouse. Brain Struct Funct. 214:339–353.

Van der Loos H, Woolsey TA. 1973. Somatosensory cortex: structural alterations following early injury to sense organs. Science. 179:395–398.

Yizhar O, Fenno LE, Davidson TJ, Mogri M, Deisseroth K. 2011. Optogenetics in neural systems. Neuron. 71:9–34.

Yona G, Meitav N, Kahn I, Shoham S. 2016. Realistic numerical and analytical modeling of light scattering in brain tissue for optogenetic applications(1,2,3). eNeuro. 3. doi: 10.1523/ENEURO.0059-15.2015.

Zhang F, Wang L-P, Brauner M, Liewald JF, Kay K, Watzke N, Wood PG, Bamberg E, Nagel G, Gottschalk A, et al. 2007. Multimodal fast optical interrogation of neural circuitry. Nature. 446:633–639.

Zhu Y, Qiao W, Liu K, Zhong H, Yao H. 2015. Control of response reliability by parvalbumin-expressing interneurons in visual cortex. Nat Commun. 6:6802.

Zucca S, D'Urso G, Pasquale V, Vecchia D, Pica G, Bovetti S, Moretti C, Varani S, Molano-Mazón M, Chiappalone M, et al. 2017. An inhibitory gate for state transition in cortex. eLife 6: e26177. doi: 10.7554/eLife.26177.